

Quantum spins and hybridization in artificially-constructed chains of magnetic adatoms on a superconductor

Eva Liebhaber,¹ Lisa M. Rütten,¹ Gaël Reecht,¹ Jacob F. Steiner,² Sebastian Rohlf,³ Kai Rossnagel,^{3,4} Felix von Oppen,² and Katharina J. Franke¹

¹*Fachbereich Physik, Freie Universität Berlin, 14195 Berlin, Germany*

²*Dahlem Center for Complex Quantum Systems and Fachbereich Physik, Freie Universität Berlin, 14195 Berlin, Germany*

³*Institut für Experimentelle und Angewandte Physik, Christian-Albrechts-Universität zu Kiel, 24118 Kiel, Germany*

⁴*Ruprecht Haensel Laboratory, Deutsches Elektronen-Synchrotron DESY, 22607 Hamburg, Germany*

(Dated: April 1, 2025)

Magnetic adatom chains on surfaces constitute fascinating quantum spin systems. Superconducting substrates suppress interactions with bulk electronic excitations but couple the adatom spins to a chain of subgap Yu-Shiba-Rusinov (YSR) quasiparticles. Using a scanning tunneling microscope, we investigate such correlated spin-fermion systems by constructing Fe chains adatom by adatom on superconducting NbSe₂. The adatoms couple entirely via the substrate, retaining their quantum spin nature. In dimers, we observe that the deepest YSR state undergoes a quantum phase transition due to Ruderman-Kittel-Kasuya-Yosida interactions, a distinct signature of quantum spins. Chains exhibit coherent hybridization and band formation of the YSR excitations, indicating ferromagnetic coupling. Longer chains develop separate domains due to coexisting charge-density-wave order of NbSe₂. Despite the spin-orbit-coupled substrate, we find no signatures of Majoranas, possibly because quantum spins reduce the parameter range for topological superconductivity. We suggest that adatom chains are versatile systems for investigating correlated-electron physics and its interplay with topological superconductivity.

INTRODUCTION

Ever since the early days of quantum mechanics, chains of coupled quantum spins have been a paradigm of strongly interacting quantum systems [1]. Magnetic adatoms on surfaces have been an attractive platform for realizing assemblies of interacting spins, also because atom manipulation allows for designing a wide variety of structures and couplings [2]. On normal-metal substrates, the adatom spins couple to and relax via the particle-hole continuum of the conduction electrons. This relaxation can be suppressed on superconducting substrates as a consequence of their excitation gap [3]. The gap effectively decouples the adatom chain from the bulk electronic excitations of the substrate, while retaining the Ruderman-Kittel-Kasuya-Yosida (RKKY) [4–6] and Dzyaloshinsky-Moriya interactions [7, 8] between adatom spins, which are mediated by higher-energy states of the quasiparticle continuum.

Despite this decoupling from bulk excitations, chains of magnetic adatoms remain intimately coupled to electronic subgap excitations localized along the chain, enabling intriguing correlated-electron physics [9]. The exchange coupling of the adatom spins to the substrate electrons induces fermionic subgap excitations within the superconducting gap known as Yu-Shiba-Rusinov (YSR) resonances [10–13]. The dynamics emerging from coupling chains of quantum spins to these fermionic YSR excitations is reminiscent of Kondo lattice systems [14] and high- T_c superconductors [15]. The physics of chains of magnetic adatoms on superconductors is further enriched by quantum phase transitions [16–20]. Reflecting the

competition between superconducting pairing and magnetic interactions, the adatom can bind different numbers of quasiparticles. The bound quasiparticles (partially) screen the adatom spin, so that these quantum phase transitions are accompanied by changes in the effective spin [16, 21]. Intriguingly, tunneling into the adatom chain at subgap bias voltages can locally bind or unbind one of these quasiparticles and thereby generate a mobile impurity [9].

Here, we build magnetic chains Fe adatom by Fe adatom on a $2H$ -NbSe₂ substrate and track their spatially resolved excitation spectra all the way from the monomer to longer chains. Quantum phase transitions induced by the RKKY coupling reveal the intimate coupling of the quantum spins of the adatoms to the fermionic subgap quasiparticles. The YSR excitations exhibit coherent hybridization along the chain and the resulting band formation as a function of chain length is consistent with ferromagnetic coupling of the adatom spins. Longer chains are affected by the charge-density-wave (CDW) order of the $2H$ -NbSe₂ substrate that coexists with superconductivity.

Previous studies of magnetic chains on superconducting substrates, motivated by the search for topological superconductivity and Majorana bound states, relied on densely-packed adatoms, formed either by self assembly [22–26] or by atom manipulation [27–31]. The theoretical description of these chains assumes classical spin structures and bands of hybridizing adatom d orbitals, which cross the Fermi level [22, 32–34]. In contrast, we construct magnetic adatom chains in the dilute limit [35], in which the adatoms are spaced sufficiently far that direct

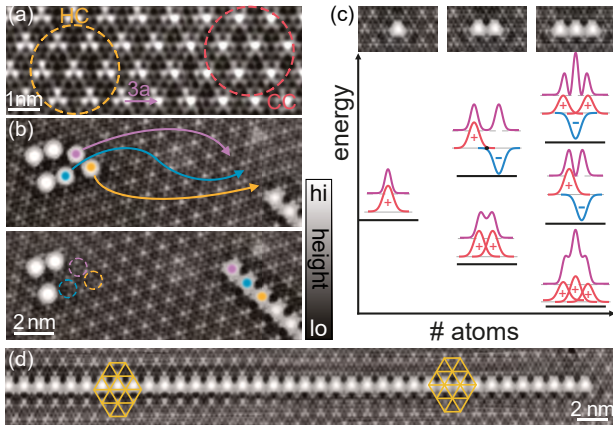


Figure 1. (a) Atomic-resolution topography of a clean NbSe₂ surface. Regions with HC (CC) CDW patterns are indicated in yellow (red). (b) Topography images illustrating the sequence of atomic-manipulation steps to obtain an Fe chain. (c) Monomer, dimer, and linear trimer of Fe atoms with schematic illustration of the hybrid YSR wave functions. (d) Topography of a long chain. The yellow grids illustrate the position of the CDW maxima relative to the atoms of the chain. Constant-current set point for all topographies 100 pA, 10 mV.

hybridization of their *d* orbitals is negligible, but close enough for substrate-mediated interactions. In this limit, the interactions between the adatoms are mediated not only by the familiar RKKY and Dzyaloshinsky-Moriya interactions but also by hybridization of the adatoms' YSR excitations as previously studied in YSR dimers [12, 36–42]. Importantly, in the dilute limit, the quantum nature of the individual adatom spins is preserved and plays an essential role when coupling adatoms into chains [9].

Such dilute chains of magnetic adatoms are not only a platform for correlated-electron physics but can also exhibit topological superconductivity and Majorana bound states [9, 35, 43–45]. However, as a consequence of the quantum spin nature and of singlet pairing correlations induced by the substrate superconductor, one expects [9] that the parameter region exhibiting topological superconductivity is considerably more limited than suggested by previous work [35] assuming classical spin textures. In fact, we do not observe signatures of Majorana end states in any of our chains. However, dilute adatom chains admit extensive flexibility in tuning the effective adatom spins, the magnetic anisotropy, or the sign and magnitude of the RKKY coupling. One can thus in principle realize a wide variety of quantum spin chains, with higher-spin adatoms promising more extensive topological superconducting phases.

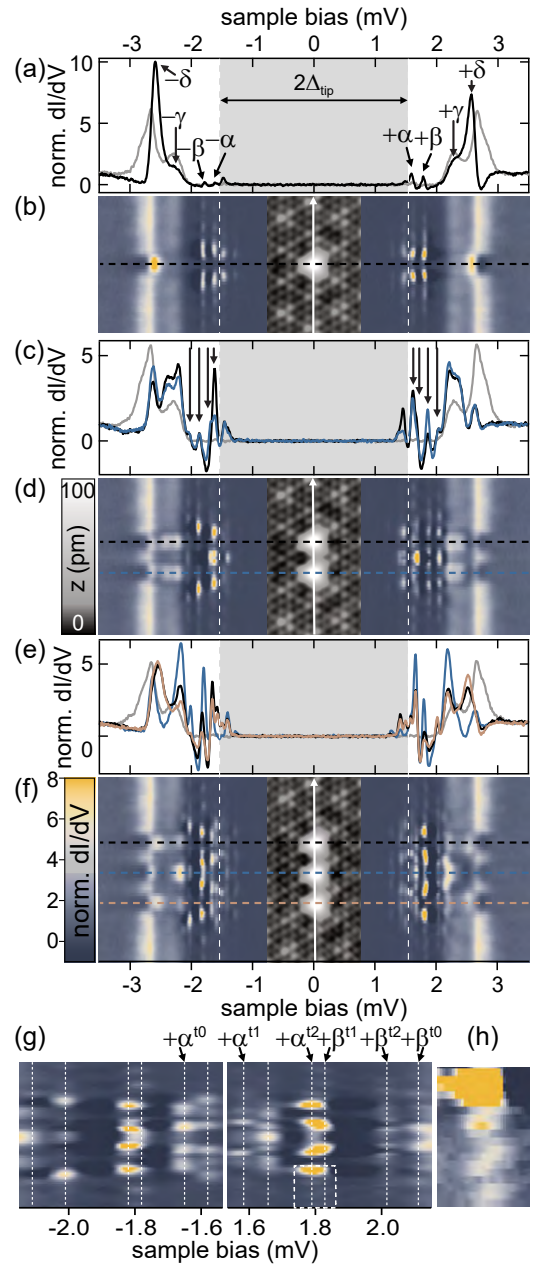


Figure 2. (a,c,e) Normalized differential conductance spectra recorded on the atoms for the monomer (a), dimer (c) and trimer (e) and on the bare NbSe₂ (gray). Tip gap indicated in gray. Feedback was opened at 250 pA, 5 mV and a modulation of 15 μ V was used. In (a) the α -, β -, γ - and δ -resonances are indicated by black arrows. In (c), the split resonances from α and β are indicated by arrows. (b,d,f) Line profiles recorded along the monomer (b), dimer (d) and trimer (f) as illustrated in the topographies (insets; recorded in constant-current mode with set point 100 pA, 10 mV). Horizontal dashed lines serve as guide to the eye for the precise location of the spectra of (a,c,e). Vertical white dashed lines indicate $2\Delta_{\text{tip}}$. (g) Zoom to subgap range of (f). The α - and β -resonances are indicated by the white dashed lines and labeled above the panels. (h) Close-up of the oscillatory decay around 1.8 mV as indicated by the box in (g).

RESULTS

Monomer

Fe atoms on NbSe₂: monomers, dimers and trimers

We build chains on the van der Waals-layered superconductor $2H$ -NbSe₂ starting with a single Fe atom and continuing all the way to a 51-atom chain. A coexisting CDW [46–48] is reflected in periodic, but weakly incommensurate height modulations with a period of $\sim 3a$, which are superimposed on the atomic corrugation (see STM image in Fig. 1a). When the CDW maximum is centered on the hollow site (hollow centered, HC), the topography exhibits a three-petaled shape (yellow area in Fig. 1a), while the Se-atom centered configuration (chalcogen centered, CC) exhibits a petalless pattern (red area). Superconductivity appears below a critical temperature of 7.2 K. The anisotropic energy gap of about 1 meV results in two-humped coherence peaks in the dI/dV spectra (see gray spectrum in Fig. 2a) [49–52].

As deposited, Fe atoms adsorb in the two distinct hollow sites of the terminating Se layer, with or without Nb atom underneath (metal centered and hollow centered, respectively). The two kinds of Fe adatoms exhibit distinct YSR spectra, reflecting different crystal-field splittings as well as exchange and potential scatterings [53]. To maximize YSR hybridization, we assemble shorter chains such that all Fe atoms are positioned on identical (hollow-centered) sites (Fig. 1b-c). The quasi-two-dimensional nature of NbSe₂ has been shown to yield extended YSR states [54, 55], thereby enabling strong YSR hybridization within our dilute chains. Kondo signatures observed for the monomer imply that individual adatoms should be considered as quantum spins, which are then coupled via hybridization of YSR states, RKKY and Dzyaloshinsky-Moriya interactions, as well as pairing correlations when adding further adatoms.

For individual Fe atoms, local variations associated with the CDW shift the energy and modify the wave functions of the YSR states [53]. Consequently, effective hybridization of YSR states requires not only that the adatoms are located at identical adsorption sites of the atomic lattice, but also at comparable positions with respect to the CDW. Here, we focus on hollow-centered Fe adatoms located on maxima with respect to the CDW by placing adatoms at a distance of $3a$. We show and exploit that with this choice, the YSR states of adjacent Fe atoms are sufficiently similar that they hybridize into symmetric and antisymmetric linear combinations (see sketch in Fig. 1c). Successively placing Fe atoms at a distance of $3a$ (Fig. 1b), we find that chains with about ten adatoms or less remain essentially uniform. Longer chains become inhomogeneous due to the incommensurate nature of the CDW (Fig. 1d).

We begin with an analysis of the monomer. YSR states have been observed in NbSe₂ for magnetic atoms located in the bulk [54, 56] and on the surface [53, 55, 57]. A differential conductance (dI/dV) spectrum of a Fe monomer at the specified adsorption site and recorded with a superconducting Nb tip is shown in Fig. 2a (black line; tip gap indicated in gray). We resolve four pairs of subgap YSR resonances labeled α - δ at symmetric bias voltages. These emerge from exchange coupling four half-filled d orbitals to corresponding conduction electron channels [58, 59], indicating that the Fe atom is in a spin-2 state.

Depending on the sign of the energy E_{YSR} of the corresponding YSR resonance, each channel can bind a quasiparticle ($E_{\text{YSR}} < 0$) or not ($E_{\text{YSR}} > 0$), with the two options separated by a quantum phase transition at $E_{\text{YSR}} = 0$ (see also SM [60]). Each bound quasiparticle partially screens the bare impurity spin $S = 2$. We can deduce the sign of the four YSR states by tracking how the energies of the YSR states shift as a function of the adsorption site relative to the CDW [53]. Our analysis indicates that at the specified adsorption site, three YSR resonances (α - γ) are in the screened state. The fourth resonance (δ) can be in the screened or in the unscreened state, with the latter possibility being more likely and assumed in the following. With three channels binding a quasiparticle at the impurity site, the impurity spin is effectively reduced to $S_{\text{eff}} = \frac{1}{2}$ in the monomer. We conclude that the monomer is in a ($Q = 3, S_{\text{eff}} = \frac{1}{2}$) ground state, where Q counts the number of bound quasiparticles. (Further indications against the less likely assignment of four screened channels are provided in the supplementary material (SM) [60].)

We can further characterize the YSR resonances through their wave-function patterns. Throughout this paper, we plot the hole-like components of the YSR wave function, which are observed at positive bias voltage for a screened spin and at negative bias voltage for an unscreened spin. (The maps of the electron-like components appearing at opposite bias voltages are shown in the SM [60].) We focus on the YSR states α and β , which lie deepest inside the gap and are most easily disentangled from the background. Corresponding spectra taken across the Fe atom along the high-symmetry direction of the substrate display long-range oscillations of the YSR wave functions (color plot in Fig. 2b), which have their highest intensity slightly away from the center of the Fe atom. Differential conductance maps of the α and β resonances exhibit overall D_3 symmetry of the YSR wave functions (brownish plots in Fig. 3a) reflecting the anisotropic Fermi surface of NbSe₂, the local crystal field, and the symmetry of the CDW [53]. In the following, the YSR wave functions provide fingerprints which

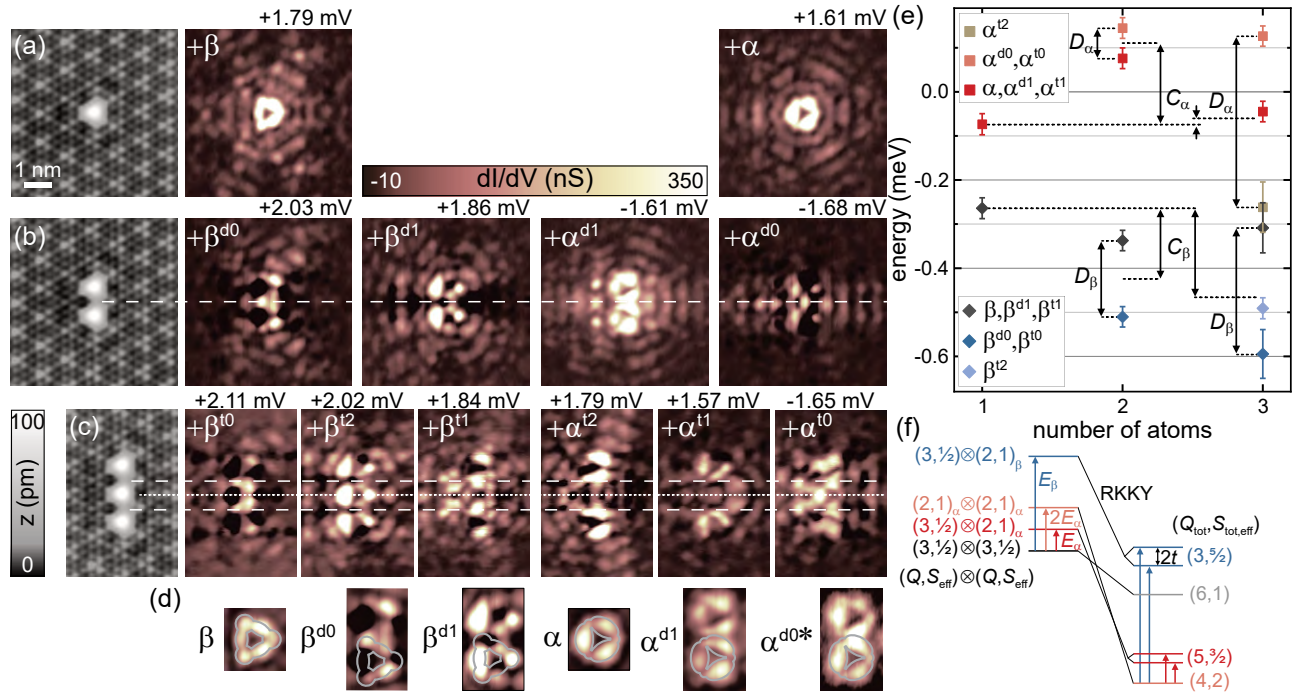


Figure 3. (a-c) STM topographies (constant-current mode with set point 100 pA, 10 mV) of one to three Fe atoms with spacing of $3a$ in the left. Corresponding constant-contour dI/dV maps of the (hybridized) YSR states in the monomer (top row), dimer (middle row) and trimer (bottom row). Constant-contour feedback was opened at 250 pA, 5 mV and a modulation of 15 μ V was used. Horizontal dashed/dotted lines serve as guide to the eye. (d) Close-ups around the atoms' center for the monomer and dimer α and β states. Gray lines serve as guide to the eye. (e) Quantitative energy evolution of the α and β states upon hybridization. Shift C relative to the monomer and splits D are indicated. Note that the CDW-induced energetic evolution of the monomer YSR states suggests α and β to be in the screened-spin regime [53], hence, implying a negative ground state energy (of the monomer states). (f) Schematic energy level diagram of the dimer. States of the uncoupled dimer (left) are labeled by (Q, S_{eff}) for both adatoms. States of the coupled dimer (right) are labeled by the total number of bound quasiparticles and effective spin, $(Q_{\text{tot}}, S_{\text{tot,eff}})$. The values of $S_{\text{tot,eff}}$ assume ferromagnetic RKKY coupling as suggested by band formation in chains (see below).

allow us to track how YSR resonances shift and hybridize as adatoms are assembled into chains.

Dimer

The small effective spin $S_{\text{eff}} = \frac{1}{2}$ of the adatoms suggests that the adatom spins couple quantum mechanically. This expectation is supported by an analysis of dimer spectra. We realize dimers by placing a second Fe atom on an adjacent maximum of the CDW at a distance of $3a$. Taking dI/dV spectra at the centers of the two atoms (black and blue lines in Fig. 2c), we now find two states each in the energy regions of the original α and β states. The doubling of the YSR states persists all along the dimer axis with oscillatory intensity distribution and overall mirror symmetry about the center of the dimer (Fig. 2d). This doubling can be naturally understood in terms of hybrid YSR states, which are symmetric and antisymmetric linear combinations of the monomer states.

We corroborate this interpretation by dI/dV maps of the YSR wave functions taken at the corresponding peak

energies in Fig. 3b. Two maps (2.03 mV and 1.86 mV) can be assigned to the hybridized β states. Apart from their energy, this is supported by the shapes of the YSR wave functions, see close-ups in Fig. 3d. The β state exhibits intensity at the sides and vertices of a triangular shape. Both features reappear in the patterns of the dimer, albeit with characteristic modifications due to hybridization. The map at 2.03 mV shows increased intensity in between the Fe atoms and is identified with the symmetric combination. The map at 1.86 mV exhibits a nodal line of suppressed intensity perpendicular to the dimer axis (dashed line in Fig. 3b), consistent with the antisymmetric combination. We label these dimer (d) states as β^{dn} , where n counts the number of nodal planes.

We also identify symmetric and antisymmetric combinations of the α states, which appear as a peak with a shoulder in spectra taken directly above the Fe atoms (Fig. 2c) and can be disentangled by the corresponding modulations along the dimer axis (Fig. 2d). For this assignment, we inspect the corresponding dI/dV maps at positive and negative bias voltage (shown in Fig. 3b and SM [60], respectively). dI/dV maps of α^{d0} and α^{d1} in-

deed lack or exhibit a nodal line perpendicular to the dimer axis. Inspection of the dI/dV pattern probed at negative bias in the close vicinity of the Fe atoms reveals shapes which are strikingly similar to the monomer's α state at positive bias voltage. This is seen most clearly from the close-ups of α as well as α^{d0*} and α^{d1} shown in Fig. 3d. (Note that for α^{d0} , we present the dI/dV map recorded at the energy of the corresponding thermal peak as indicated by the asterisk in α^{d0*} , because the map at α^{d0} is strongly influenced by the negative differential conductance of α^{d1} , see SM [60]). This reflects that the α state has crossed the quantum phase transition upon dimer formation. In the monomer, the α state is screened and its hole-like wavefunction is observed at positive bias. If the α states cross the quantum phase transition and are unscreened in the dimer, its hole wave functions – corresponding to symmetric and antisymmetric combinations of the monomer's hole wave function – are observed at negative bias.

The crossing of the quantum phase transition between monomer and dimer requires a substantial shift of the α state, in addition to the hybridization splitting. Moreover, this shift is opposite to that of the β state, which moves toward the gap edge in the dimer (see Fig. 3e for a quantitative analysis of the shift (C) and splitting (D) based on deconvolved dI/dV spectra shown in SM [60]). Previous works [37, 40] have analyzed these shifts and splittings in terms of a classical-spin model. However, neither shifts larger than the splitting nor shifts in opposite directions for different YSR states appear naturally in this model (see theoretical considerations in SM [60] for further discussion).

Importantly, these behaviors can be understood for quantum spins coupled via RKKY interactions and hybridization. While unbinding the quasiparticles bound in the α channel costs YSR energy, it also increases the effective impurity spins from $S_{\text{eff}} = \frac{1}{2}$ to $S_{\text{eff}} = 1$ and hence the gain in RKKY energy. On balance, it can thus be energetically favorable in the dimer to unbind the quasiparticles.

This is further illustrated in the schematic level diagram shown in Fig. 3f, which emphasizes the effects of RKKY coupling and hybridization by showing the states of the uncoupled dimer on the left and of the coupled dimer on the right. In the ground state of the uncoupled dimer, both adatoms are in the ($Q = 3, S_{\text{eff}} = \frac{1}{2}$) state. Exciting the α or β resonance of one of the adatoms excites it into ($Q = 2, S_{\text{eff}} = 1$) states. When only one of the two adatoms is excited, there are two degenerate states of the uncoupled dimer, which are split in the coupled dimer by the YSR hybridization. Such a splitting does not exist for states in which both adatoms are in the same state, resulting in a nondegenerate configuration. In addition to the splittings, there is a downward shift of the energies of the coupled dimer due to the RKKY interaction. This shift tends to be larger for larger S_{eff} .

Thus, as illustrated in Fig. 3f, the ground state of the coupled dimer can emerge from an excited state of the uncoupled dimer, consistent with our observation of a quantum phase transition of the α resonance from the monomer to the dimer.

The gain in RKKY energy is a consequence of the quantum nature of the adatom spins and has no analog in classical-spin models (see also SM [60]). In a quantum model, screening the adatom spin changes its state. For instance, when screening a spin- $\frac{1}{2}$ impurity, it forms a singlet with the quasiparticle spin and no longer points in a preferred direction. This contrasts with classical-spin models, in which the impurity spin remains aligned along a certain direction, merely binding a quasiparticle with antiparallel spin.

Trimer

Forming a trimer by deliberately adding a third atom at a distance of $3a$, we now identify three states each in the α and β regions (see spectra in Fig. 2e,f). We can again disentangle the underlying hybrid states based on energy considerations, the intensity modulations of the split states along the trimer axis (see close-ups in Fig. 2g,h), and their corresponding dI/dV maps (Fig. 3c; in addition to the number n of nodal planes, we label the trimer by t). Despite the complexity of the patterns due to the oscillatory nature of the YSR wave functions, we tentatively identify the number of nodal planes perpendicular to the trimer axis in the individual maps of the YSR resonances. In the maps at 1.57 mV and 1.84 mV, we find a single nodal plane at the center of the trimer marked by a dotted line. Two nodal planes between the Fe atoms, marked by dashed lines, are clearly seen in the map at 2.02 mV and less pronounced at 1.79 mV (see also maps at negative bias in SM [60]). The latter state is very close in energy to the state at 1.84 mV and may thus be partially obscured. The maps at 2.11 mV and -1.65 mV lack clear evidence of nodal planes. We can now assign resonances to α and β (see Fig. 3c) based on their energy, supported by a comparison of structural elements of their maps to monomer and dimer. In particular, the near field of β^{t2} closely resembles the ones of β and β^{d1} . We note that we assign the binding energy of the resonance α^{t0} to have opposite sign relative to the others. This assignment is corroborated by the observation that during band formation with increasing chain length, α -derived states appear near zero energy (see below).

Our tentative assignments allow us to track the energy shifts and splittings from deconvolved data, which we find to be consistent with the scenario of quantum spins subject to RKKY interactions and hybridization (Fig. 3e). While the RKKY interaction leads to further shifts, hybridization increases the number of states. Importantly, the energy of the hybrid β states is not monotonous with

the number of nodal planes as we find the β^{t2} state in the energetic center of the respective triplet structure. This change in energetic order can be rationalized by accounting for next-nearest-neighbor RKKY interactions.

Evolution of YSR bands in Fe atom chains

The importance of next-nearest-neighbor couplings is also evident in longer Fe chains. Figure 4a-h shows chains made up of $N = 4-11$ Fe atoms (the atom added last is marked in red) and corresponding dI/dV spectra along their entire lengths. Neighboring atoms are placed at a distance of $3a$, and all adsorption sites remain close to the CDW maximum. We note that the adatoms may help to lock the CDW to the underlying atomic lattice over longer distances than for the pristine surface (cf. Fig. 1a and d).

In the shorter chains, we observe strong modifications of the subgap spectra with the addition of every atom. These modifications become less pronounced with increasing chain length. In the presence of next-nearest-neighbor interactions, the two outermost atoms at either end of the chain are subject to different interactions from the central atoms (Fig. 4i). Thus, beginning only with $N = 5$ atoms, the chains develop a uniform central region which will eventually lead to the formation of YSR bands [61].

Consistent with this picture, the subgap structure of the quadrumer (Fig. 4a) differs drastically from that of the trimer (Fig. 2f). The α and β states of the monomer are now expected to form four hybrid states each. A detailed assignment, however, becomes increasingly difficult with growing chain length as the hybrid states are overlapping within our energy resolution. Attaching a fifth atom causes yet another strong modification of the subgap structure (Fig. 4b). For instance, unlike for $N = 4$, we now observe a delocalized state of α character at zero energy (i.e., at a bias of $\sim \pm 1.55$ mV corresponding to the tip gap). Apart from the atomic corrugation, this state has a nodeless intensity distribution exhibiting highest spectral weight at the center of the chain and falling off toward both ends (left red arrow, Fig. 4b, dI/dV maps are provided in SM [60]). Furthermore, there are several resonances around ± 1.7 mV which are absent for $N = 4$, with one state exhibiting strong intensity at the chain ends (right red arrow).

Upon addition of another Fe atom ($N = 6$), the zero-energy state is shifted to slightly higher energies. At $\sim \pm 1.7$ mV there is a very weak resonance with different spatial fingerprints (no intensity at the chain terminations) as opposed to $N = 5$ (Fig. 4c). While we cannot characterize all states individually, the concerted variation of the subgap structure along the entire chain indicates coherent coupling of all YSR states. This remains valid for the longer chains, for which broader features

seem to converge into the specific energy intervals indicated by vertical dotted lines (Fig. 4) within the uniform center of the chain (horizontal dashed lines in panels g,h). This behavior is consistent with the formation of YSR bands based on the original α and β states of the monomer. Once the bands are fully developed, their van Hove singularities become the strongest features in the dI/dV spectra.

We suggest that the β -derived band extends from the center to the edge of the superconducting gap (solid and dashed blue lines in sketch of Fig. 4j for electron-like and hole-like bands, respectively). This assignment is based on tracking the uppermost and lowermost hybrid states of β -character in the dI/dV maps (see SM [60]). The determination of the width of the α -derived band demands tracking the complete evolution of its parent states with increasing chain length. The presence of α -derived states close to the Fermi level at intermediate chain lengths requires the α -derived band to cross the Fermi level, with the upper van Hove singularity at ~ 1.7 mV for the electron-like band. The identification of the lower band limit is less unequivocal. As we observe only three possible van Hove singularities (at fixed bias polarity), the α -derived band may either lie symmetrically about the Fermi level with band edges at $\sim \pm 1.7$ mV or reach down to the upper van Hove singularity of the β -derived band (red line in Fig. 4j). The latter scenario is more natural in view of the large observed splitting of the α states in the trimer (cf. Fig. 3f). (To show the α -like character of the bands, we present several dI/dV maps in SM [60].)

The crossing of the Fermi energy by the α -derived band requires sufficiently strong hybridization, possibly including next-nearest-neighbor contributions [62]. This was already present in the trimer structure, where we assigned the α^{t0} state to the opposite side of the Fermi energy as $\alpha^{t1,t2}$. Crossing of YSR bands through the Fermi level is a necessary requirement for realizing topological superconductivity and Majorana end states [32, 35]. Here, we neither find signatures of Majoranas nor of the required opening of a p -wave gap around the Fermi energy. The observation of a zero-energy state localized at the chain ends for $N = 10$ (Fig. 4g, red ellipses) disappears upon addition of another Fe atom (Fig. 4h) and should thus be attributed to small spectral changes for finite chains (see SM [60] for dI/dV maps).

The formation of YSR bands and van Hove singularities suggests that the adatom spins couple ferromagnetically. Exciting a YSR resonance by tunneling into the quantum spin chain locally modifies the effective spin [9]. For instance, exciting the (screened) β resonance increases the effective spin of the local adatom by $1/2$, introducing a mobile impurity into the spin chain. For a ferromagnetic spin background, the mobile impurity effectively forms a single-particle band with van Hove singularities. As illustrated by a model calculation for a spin- $\frac{1}{2}$ chain shown in SM [60], other spin orders typ-

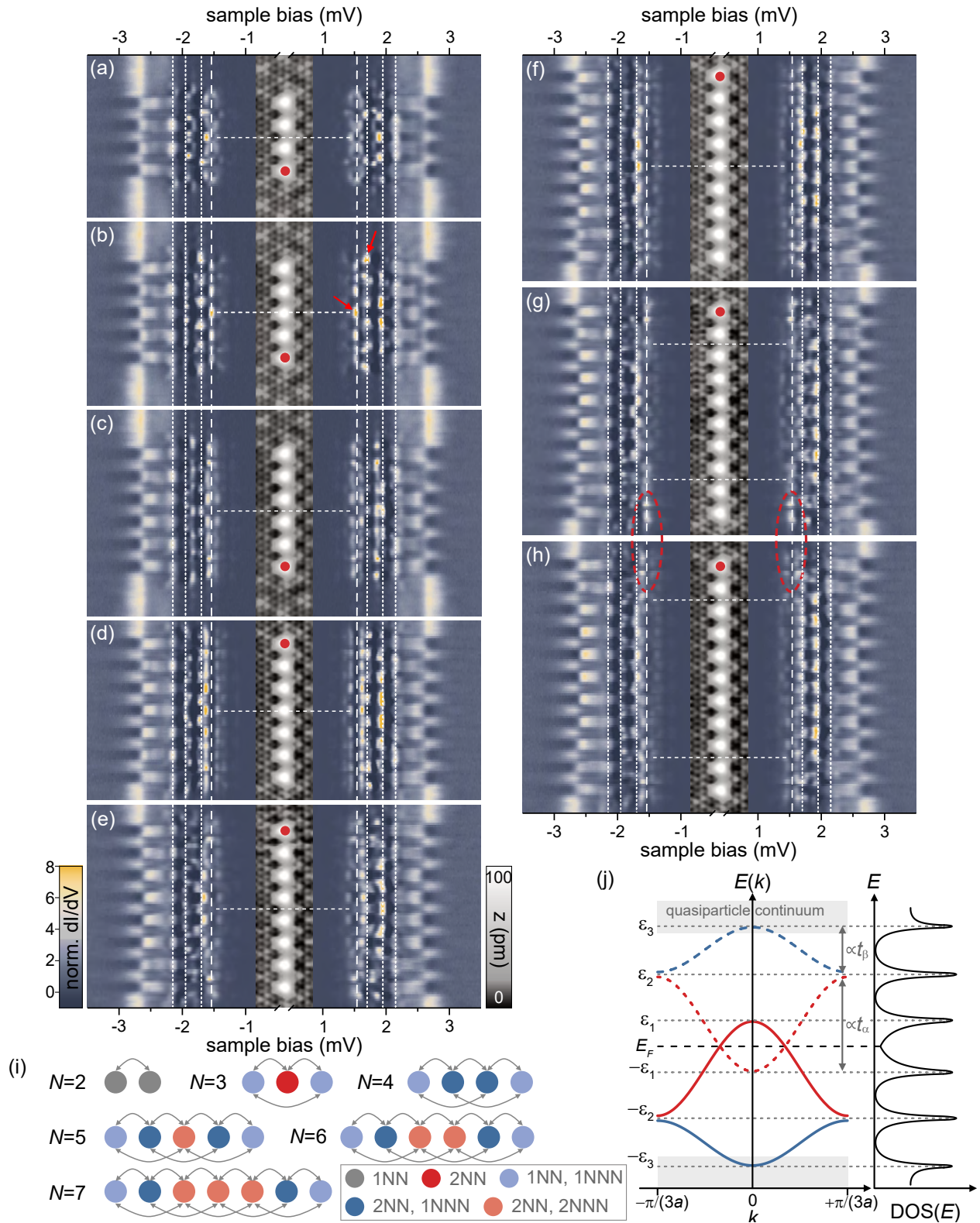


Figure 4. Stacked constant-height dI/dV spectra (normalized) recorded along lines across chains containing 4-11 atoms (a-h) as illustrated in the inset topographies (constant-current mode with set point 100 pA, 10 mV). Set point for spectra 250-700 pA, 5 mV with a modulation of 15 μ V. Vertical dashed and dotted lines indicate $\Delta_{\text{tip}} \approx \pm 1.55$ meV and ± 2.15 meV, ± 1.95 meV and ± 1.7 meV corresponding to energies of ± 0.6 meV, ± 0.4 meV and ± 0.15 meV, respectively. Horizontal dashed lines in (a-f) indicate mirror symmetry axes perpendicular to the chain. Horizontal dashed lines in (g,h) delimit the homogeneously appearing bulk of the chain. The states at the chain's termination are marked by a red ellipse. Red dots mark the atom, that is added to the chain. Red arrows in (b) mark the large intensity at the center of the chain (left) and at the chain's termination (right), see text. (i) Schematic illustration of the number of (next) nearest (N)NN neighbors for different atoms in chains with different lengths. (j) Schematic illustration of band formation and DOS with van Hove singularities at band edges. $\pm \epsilon_{1,2,3}$ correspond to the three pairs of dotted lines in (a-h). The solid (dashed) lines represent the dispersion of the electron-like (hole-like) bands of the α (red) and β (blue) bands.

ically exhibit more involved excitation spectra. Consistent with our observations, these model calculations also exhibit strong spectral variations as a function of N for short chains which eventually evolve into band-like behavior in longer chains.

Longer Fe chains and CDW

As the chains grow beyond $N = 11$, the CDW becomes increasingly relevant. Due to the incommensuration, the atoms can no longer all sit on maxima of the CDW. dI/dV spectra recorded along a 27-atom chain (Fig. 5a) show spatial variations of the YSR band structure. This is clearly reflected in the breaking of the overall mirror symmetry about the center of the chain, which was present in the shorter chains (cf. horizontal dashed lines in Fig. 4a-f). In addition, the YSR bands that are within the quasiparticle coherence peaks in region B (indicated in Fig. 5a) shift continuously toward the Fermi level at both ends of the chain (more pronounced in region C than in region A). In the center of the chain (region B), the spectra are similar to those of the 11-atom chain (original 11-atom chain is indicated by yellow circles). In particular, the bands originating from the α and β states (marked by white dotted lines) appear as in the shorter chain. dI/dV maps at selected energies reflect this dispersion (Fig. 5d; for a more complete set of dI/dV maps, see SM [60]). For instance, the highest-energy feature appears at 2.50 mV in region B, but at 2.26 mV in regions A and C. The van Hove singularity at ~ 1.95 mV appears at the same energy almost along the entire chain (map at 1.94 mV). Similarly, the van Hove singularity of the α -derived band at -1.70 mV exhibits a small shift towards zero energy only at the terminations (see map at 1.54 mV and SM [60] for maps at negative bias).

The energy shifts of the YSR bands can be correlated with changes of the CDW along the chain (Fig. 5b,c). The CDW appears as apparent height modulations beyond the atomic corrugation in the STM topography in Fig. 5b (covering a wider region on both sides of the chain). To highlight the CDW, we remove the atomic lattice from the STM image by Fourier filtering (Fig. 5c) and connect maxima of the CDW by black dashed lines (shown only in the left side of the chain for clarity). In region A, the CDW is distorted by the dark defect visible at the top. In region B, the CDW is parallel and appears locked to the atomic lattice (3a), so that all Fe atoms are located on CDW maxima. In region C, the CDW does not run parallel to the chain (see additional dashed line), resulting in variations in the adsorption sites of the Fe atoms with respect to the CDW. As shown previously [53], such changes in the adsorption site shift the YSR states of individual Fe atoms due to variations in the density of states and the potential scattering. Corre-

spondingly, the incommensurate nature of the CDW imposes a smoothly varying potential onto the YSR bands, which causes the YSR bands to shift. Interestingly, the YSR bands close to the superconducting gap edge appear to be more strongly affected.

The bands eventually shift to zero energy, which gives rise to zero-energy intensity peaks at the chain's ends. These peaks emerge from the shift in the bands and, thus, they should not be interpreted as Majoranas. Figure 6 shows a 51-atom chain, which was created by adding Fe atoms to the original 27-atom chain in regions D-E. While the CDW in region C changed during manipulation, the dI/dV spectra along the chain remain unchanged in regions A and B (see also dI/dV maps in SM [60]).

The dI/dV spectra in region D and E differ significantly from those in region B. Here, the Fe atoms are located on CDW minima as indicated by yellow triangles in the Fourier-filtered topography in Fig. 6b. This strongly modifies the YSR band structure, which now emerges by hybridizing YSR states of atoms adsorbed at minima of the CDW. Slow variations of the bands can again be attributed to changes in the relative alignment of the CDW phase, with the Fourier-filtered image revealing local distortions of the CDW pattern (most pronounced defects encircled by black dashed lines).

DISCUSSION

Dilute chains of magnetic adatoms on superconductors are qualitatively distinct from dense adatom chains which were previously investigated in searches for topological superconductivity and Majorana bound states and in which bands of adatom d orbitals are believed to cross the Fermi energy of the substrate superconductor. In dilute chains, the quantum spins associated with magnetic adatoms induce subgap quasiparticle excitations, and the substrate-induced coupling between adatoms involves spin-spin coupling via the RKKY and Dzyaloshinsky-Moriya interactions as well as hybridization of subgap quasiparticle excitations. As a result, dilute chains provide an intriguing model system probing the correlated dynamics of the quantum spins of the adatoms and the fermionic subgap quasiparticles.

We have realized such chains using atom manipulation with the STM tip, placing Fe atoms such that they reside on maxima of the CDW, and have probed the spatially resolved excitation spectra all along these chains. By carefully analyzing the subgap spectra exploiting both the YSR energies and YSR wave functions, we uncover evidence for the interactions between quantum spins and fermionic subgap excitations. In particular, we find that RKKY interactions are instrumental in inducing a quantum phase transition. The underlying competition between the energy of the YSR excitation and the RKKY coupling between adatom spins ex-

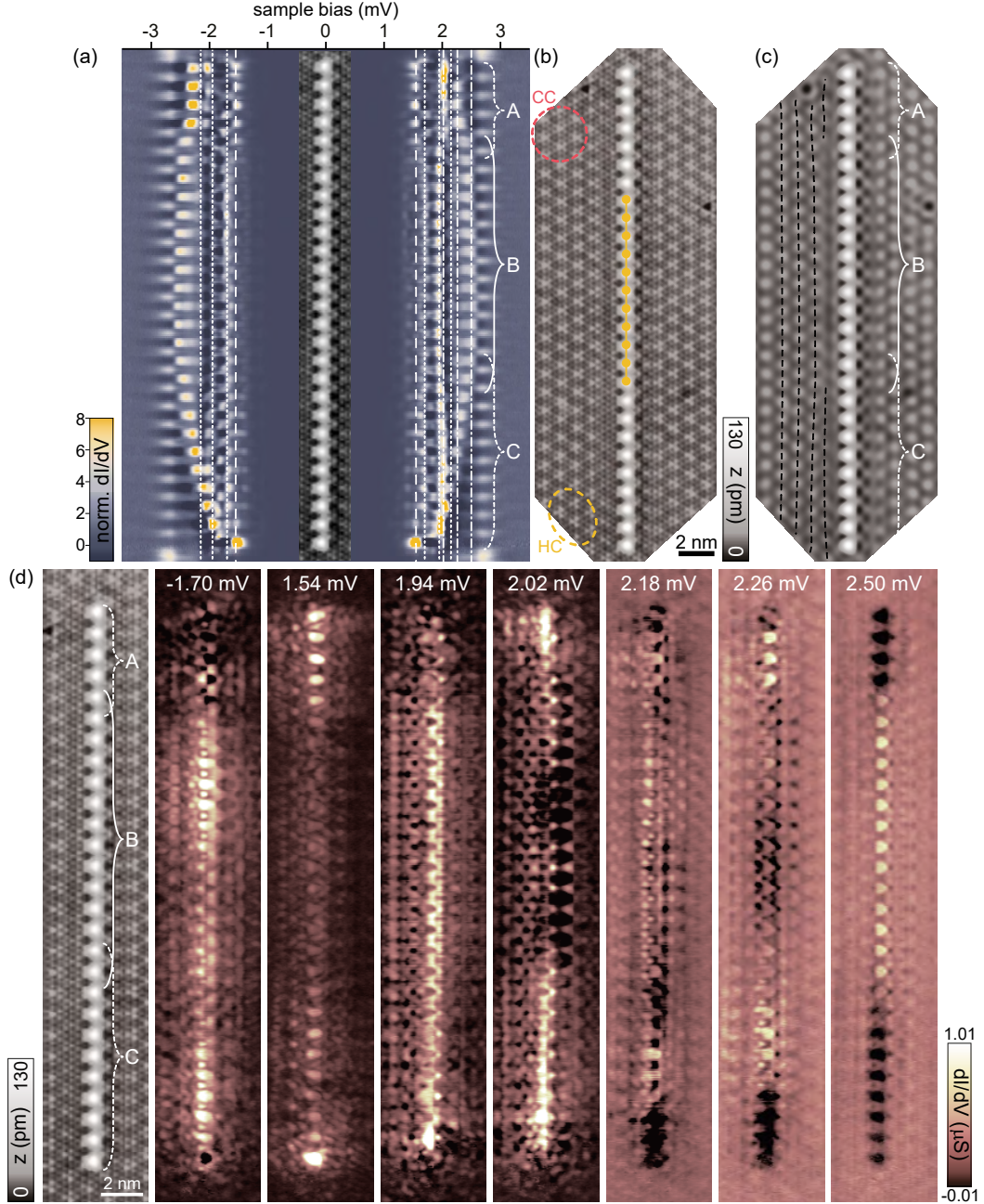


Figure 5. (a) Stacked constant-height dI/dV spectra (normalized) recorded along a line across the 27-atom chain as illustrated in the inset topography. Set point for the spectra is 700 pA, 5 mV with a modulation of 15 μ V. The (Nb) tip gap $\Delta_{\text{tip}} \approx 1.55$ meV is indicated by white dashed lines. White dotted lines are at the same energies as in Fig. 4 and indicate the van Hove singularities of the α - and β -derived bands. Dashed-dotted lines indicate additional energies of the dI/dV maps in (d). (b) Larger range STM topography of the 27-atom chain. The position of the former 11-atom chain (Fig. 4h) is indicated in yellow (constant-current set point is 100 pA, 10 mV). One region with HC (CC) CDW pattern is highlighted in yellow (red). (c) A FFT-filter has been applied to the STM topography in (b) to remove the atomic corrugation. Dashed lines on the left of the chain serve as guide to the eye to illustrate the CDW order in the vicinity of the chain. (d) STM topography of the 27-atom chain on the left. Corresponding constant-contour dI/dV maps at selected energies in the right. Constant-contour feedback was opened at 700 pA, 5 mV and a modulation of 15 μ V was used. Maps recorded at energies not already covered by white dashed or dotted lines are indicated by the dashed-dotted lines in (a). Note that there are more lines than maps as the white dotted and dashed lines point out the two low-energy bands and the tip gap, for clarity. Different sections of the chain are labeled with A-C.

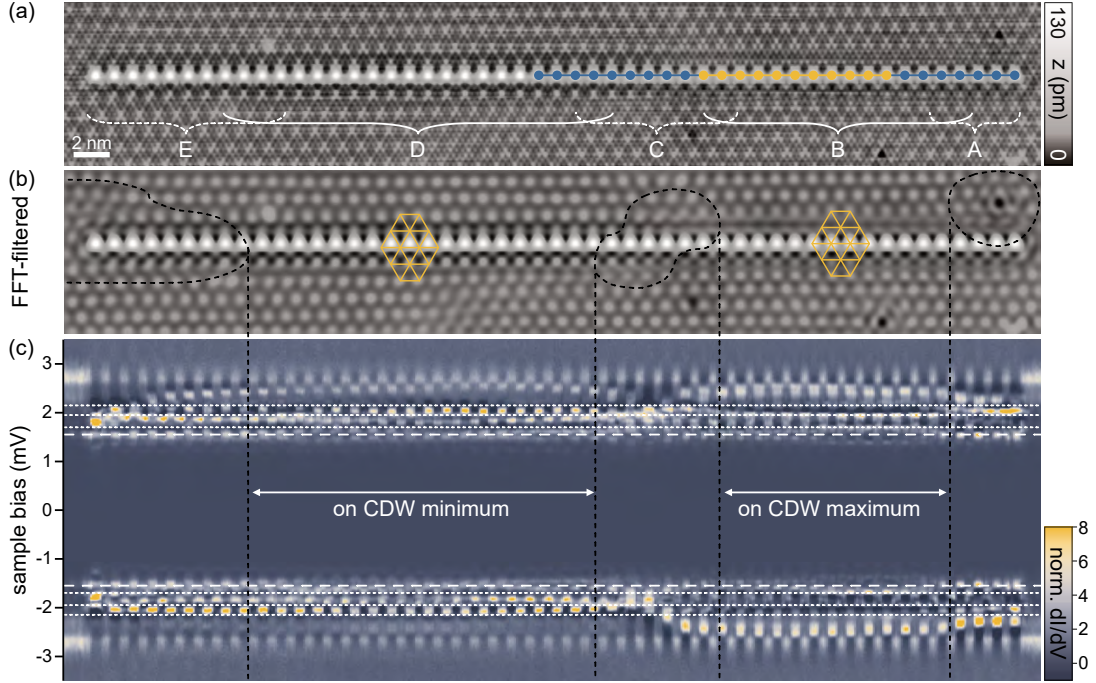


Figure 6. (a) STM topography (constant-current mode with set point 100 pA, 10 mV) of the 51-atom chain. The position of the former 11 (27)-atom chain (Figs. 4h and 5) is indicated in yellow (blue). Different sections of the chain are labeled with A-E. Sections A and B are identical to Fig. 5. (b) To remove the atomic corrugation of the STM image (a) was FFT-filtered. Dashed lines serve as guide to the eye to illustrate CDW distortions in the background. The yellow grids indicate the CDW and the positions of atoms within the chain relative to the CDW: crossings of the lines lie on CDW maxima, upwards pointing triangles on CDW minima. (c) Stacked constant-height dI/dV spectra (normalized) recorded along a line across the 51-atom chain (set point 700 pA, 5 mV with a modulation of 15 μ V). The tip gap $\Delta_{\text{tip}} \approx 1.55$ meV is indicated by dashed lines. The dotted lines are located at the same energies as in Fig. 4.

ists only for quantum spins and is absent for classical-spin models. Moreover, our observation of hybridization extending throughout longer chains and the ensuing band formation suggests that the coupling between adatom spins is ferromagnetic. Our results therefore confirm that dilute chains of magnetic adatoms are not only interesting as potential platforms for the observation of Majorana bound states, but also as highly flexible realizations of a broad class of correlated spin-fermion systems. Clearly, this is not restricted to chains, but could be readily extended to two-dimensional arrangements. In both cases, it might be particularly interesting to realize antiferromagnetic RKKY coupling by judiciously adjusting the inter-adatom distance.

The incommensurate nature of the CDW in NbSe₂ does not play a significant role up to intermediate chain lengths ($\lesssim 10$ nm) as the Fe atoms help to lock the phase of the CDW into registry with the chain. It is only with increasing chain length that the energy stored in these distortions of the CDW can no longer be sustained, triggering an abrupt change of the CDW into a different phase. Adatom chains extending across CDW domain walls exhibit significantly different band structures. In regions of a smooth change of the CDW, the YSR bands are subject to a smoothly varying potential, inducing a continuous energy shift. More generally, one can exploit substrates structured by charge density waves or by moiré lattices to investigate domain walls between different parameter regimes of the spin chain.

Although magnetic order is intrinsically fragile at finite temperatures, it would clearly be highly desirable to complement our experiments by spin-resolved STM measurements. Normal-metal-based magnetic tips have much lower resolution, making it difficult to resolve the spin polarization of the subgap resonances. A promising path forward would exploit a superconducting tip with magnetic impurity. For sufficiently strong single-ion anisotropy, the spin polarization of the resulting YSR state can be stabilized by a magnetic field (in turn requiring mono- or few-layer NbSe₂ for stability of the superconducting phase), providing a magnetic tip suitable for high-resolution measurements [63].

METHODS

Bulk 2H-NbSe₂ crystals were grown by iodine vapor transport [49] and cleaved under ultra-high vacuum conditions. Fe atoms were deposited on the freshly cleaved sample at temperatures below 15 K. Scanning tunneling microscopy and spectroscopy experiments were performed at < 1.2 K. We used superconducting Nb tips with a superconducting energy gap of $\Delta_{\text{tip}} \approx 1.55$ meV. These were prepared by indenting a NbTi wire into a Nb(111) substrate. The superconducting tip effectively increases the energy resolution beyond the temperature-

limited Fermi-Dirac distribution. The convolution of tip and sample density of states leads to a shift of all spectral features by the tip's energy gap. We deconvolve the spectra as described in the Supplementary Material of Ref. [53]. Importantly, Nb tips are suitable for controlled atom manipulation, which allows for atom-by-atom construction of the Fe chains on the NbSe₂ substrate and for tracing the spectral evolution upon chain extension.

ACKNOWLEDGEMENTS

We acknowledge discussions with C. Mora as well as financial support by Deutsche Forschungsgemeinschaft through grant CRC 183 (project C03), by the European Research Council through the consolidator grant "NanoSpin", and by the IMPRS "Elementary Processes in Physical Chemistry".

-
- [1] H. Bethe, *Z. Phys.* **71**, 205 (1931).
 - [2] D.-J. Choi, N. Lorente, J. Wiebe, K. von Bergmann, A. F. Otte, and A. J. Heinrich, *Rev. Mod. Phys.* **91**, 041001 (2019).
 - [3] B. W. Heinrich, L. Braun, J. I. Pascual, and K. J. Franke, *Nat. Phys.* **9**, 765 (2013).
 - [4] M. A. Ruderman and C. Kittel, *Phys. Rev.* **96**, 99 (1954).
 - [5] T. Kasuya, *Prog. Theor. Phys.* **16**, 45 (1956).
 - [6] K. Yosida, *Phys. Rev.* **106**, 893 (1957).
 - [7] I. Dzyaloshinsky, *J. Phys. Chem. Solids* **4**, 241 (1958).
 - [8] T. Moriya, *Phys. Rev.* **120**, 91 (1960).
 - [9] J. F. Steiner, C. Mora, K. J. Franke, and F. von Oppen, (2021), [arXiv:2107.00031](https://arxiv.org/abs/2107.00031) [cond-mat.supr-con].
 - [10] L. Yu, *Acta Phys. Sin.* **21**, 75 (1965).
 - [11] H. Shiba, *Prog. Theor. Phys.* **40**, 435 (1968).
 - [12] A. I. Rusinov, *JETP Lett.* **9**, 85 (1969).
 - [13] A. V. Balatsky, I. Vekhter, and J. X. Zhu, *Rev. Mod. Phys.* **78**, 373 (2006).
 - [14] H. Tsunetsugu, M. Sigrist, and K. Ueda, *Rev. Mod. Phys.* **69**, 809 (1997).
 - [15] P. A. Lee, N. Nagaosa, and X.-G. Wen, *Rev. Mod. Phys.* **78**, 17 (2006).
 - [16] A. Sakurai, *Prog. Theor. Phys.* **44**, 1472 (1970).
 - [17] K. J. Franke, G. Schulze, and J. I. Pascual, *Science* **332**, 940 (2011).
 - [18] L. Farinacci, G. Ahmadi, G. Reecht, M. Ruby, N. Bogdanoff, O. Peters, B. W. Heinrich, F. von Oppen, and K. J. Franke, *Phys. Rev. Lett.* **121**, 196803 (2018).
 - [19] L. Malavolti, M. Briganti, M. Hänze, G. Serrano, I. Cimatti, G. McMurtrie, E. Otero, P. Ohresser, F. Totti, M. Mannini, R. Sessoli, and S. Loth, *Nano Lett.* **18**, 7955 (2018).
 - [20] H. Huang, R. Drost, J. Senkpiel, C. Padurariu, B. Kubala, A. L. Yeyati, J. C. Cuevas, J. Ankerhold, K. Kern, and C. R. Ast, *Commun. Phys.* **3**, 199 (2020).
 - [21] R. Zitko, O. Bodensiek, and T. Pruschke, *Phys. Rev. B* **83**, 054512 (2011).
 - [22] S. Nadj-Perge, I. K. Drozdov, J. Li, H. Chen, S. Jeon, J. Seo, A. H. MacDonald, B. A. Bernevig, and A. Yazdani,

- Science* **346**, 602 (2014).
- [23] M. Ruby, F. Pientka, Y. Peng, F. von Oppen, B. W. Heinrich, and K. J. Franke, *Phys. Rev. Lett.* **115**, 197204 (2015).
- [24] B. E. Feldman, M. T. Randeria, J. Li, S. Jeon, Y. Xie, Z. Wang, I. K. Drozdov, B. Andrei Bernevig, and A. Yazdani, *Nat. Phys.* **13**, 286 (2016).
- [25] R. Pawlak, M. Kisiel, J. Klinovaja, T. Meier, S. Kawai, T. Glatzel, D. Loss, and E. Meyer, *npj Quantum Information* **2**, 10.1038/npjqi.2016.35 (2016).
- [26] M. Ruby, B. W. Heinrich, Y. Peng, F. von Oppen, and K. J. Franke, *Nano Lett.* **17**, 4473 (2017).
- [27] H. Kim, A. Palacio-Morales, T. Posske, L. Rózsa, K. Palotás, L. Szunyogh, M. Thorwart, and R. Wiesendanger, *Science Adv.* **4**, eaar5251 (2018).
- [28] L. Schneider, S. Brinker, M. Steinbrecher, J. Hermenau, T. Posske, M. dos Santos Dias, S. Lounis, R. Wiesendanger, and J. Wiebe, *Nature Commun.* **11**, 4707 (2020).
- [29] C. Mier, J. Hwang, J. Kim, Y. Bae, F. Nabeshima, Y. Imai, A. Maeda, N. Lorente, A. Heinrich, and D.-J. Choi, Atomic manipulation of in-gap states on the β - Bi_2Pd superconductor (2021), [arXiv:2104.06171](https://arxiv.org/abs/2104.06171) [cond-mat.supr-con].
- [30] L. Schneider, P. Beck, J. Neuhaus-Steinmetz, T. Posske, J. Wiebe, and R. Wiesendanger, Controlled length-dependent interaction of majorana modes in yu-shiba-rusinov chains (2021), [arXiv:2104.11503](https://arxiv.org/abs/2104.11503) [cond-mat.supr-con].
- [31] L. Schneider, P. Beck, T. Posske, D. Crawford, E. Mascot, S. Rachel, R. Wiesendanger, and J. Wiebe, Evidence of topological shiba bands in artificial spin chains on superconductors (2021), [arXiv:2104.11497](https://arxiv.org/abs/2104.11497) [cond-mat.supr-con].
- [32] S. Nadj-Perge, I. K. Drozdov, B. A. Bernevig, and A. Yazdani, *Phys. Rev. B* **88**, 020407 (2013).
- [33] J. Li, H. Chen, I. K. Drozdov, A. Yazdani, B. A. Bernevig, and A. H. MacDonald, *Phys. Rev. B* **90**, 235433 (2014).
- [34] Y. Peng, F. Pientka, L. I. Glazman, and F. von Oppen, *Phys. Rev. Lett.* **114**, 106801 (2015).
- [35] F. Pientka, L. I. Glazman, and F. von Oppen, *Phys. Rev. B* **88**, 155420 (2013).
- [36] N. Y. Yao, C. P. Moca, I. Weymann, J. D. Sau, M. D. Lukin, E. A. Demler, and G. Zaránd, *Phys. Rev. B* **90**, 241108 (2014).
- [37] M. Ruby, B. W. Heinrich, Y. Peng, F. von Oppen, and K. J. Franke, *Phys. Rev. Lett.* **120**, 156803 (2018).
- [38] D.-J. Choi, C. G. Fernández, E. Herrera, C. Rubio-Verdú, M. M. Ugeda, I. Guillamón, H. Suderow, J. I. Pascual, and N. Lorente, *Phys. Rev. Lett.* **120**, 167001 (2018).
- [39] P. Beck, L. Schneider, L. Rózsa, K. Palotás, A. Lászlóffy, L. Szunyogh, J. Wiebe, and R. Wiesendanger, *Nature Commun.* **12**, 2040 (2021).
- [40] H. Ding, Y. Hu, M. T. Randeria, S. Hoffman, O. Deb, J. Klinovaja, D. Loss, and A. Yazdani, *Proc. Nat. Acad. Sci.* **118**, e2024837118 (2021).
- [41] A. Kamlapure, L. Cornils, R. Zitko, M. Valentyuk, R. Mozara, S. Pradhan, J. Fransson, A. I. Lichtenstein, J. Wiebe, and R. Wiesendanger, Investigation of the yu-shiba-rusinov states of a multi-impurity kondo system (2019), [arXiv:1911.03794](https://arxiv.org/abs/1911.03794) [cond-mat.supr-con].
- [42] F. Küster, S. Brinker, S. Lounis, S. S. P. Parkin, and P. Sessi, Long range and highly tunable coupling between local spins coupled to a superconducting condensate (2021), [arXiv:2106.14932](https://arxiv.org/abs/2106.14932) [cond-mat.supr-con].
- [43] K. Pöyhönen, A. Westström, J. Röntynen, and T. Ojanen, *Phys. Rev. B* **89**, 115109 (2014).
- [44] F. Pientka, Y. Peng, L. Glazman, and F. von Oppen, *Phys. Scr.* **2015**, 014008 (2015).
- [45] R. Pawlak, S. Hoffman, J. Klinovaja, D. Loss, and E. Meyer, *Prog. Part. Nucl. Phys.* **107**, 1 (2019).
- [46] C. D. Malliakas and M. G. Kanatzidis, *J. Am. Chem. Soc.* **135**, 1719 (2013).
- [47] J. Dai, E. Calleja, J. Alldredge, X. Zhu, L. Li, W. Lu, Y. Sun, T. Wolf, H. Berger, and K. McElroy, *Phys. Rev. B* **89**, 165140 (2014).
- [48] C. J. Arguello, S. P. Chockalingam, E. P. Rosenthal, L. Zhao, C. Gutiérrez, J. H. Kang, W. C. Chung, R. M. Fernandes, S. Jia, A. J. Millis, R. J. Cava, and A. N. Pasupathy, *Phys. Rev. B* **89**, 235115 (2014).
- [49] D. J. Rahn, S. Hellmann, M. Kalläne, C. Sohrt, T. K. Kim, L. Kipp, and K. Rossnagel, *Phys. Rev. B* **85**, 224532 (2012).
- [50] T. Yokoya, T. Kiss, A. Chainani, S. Shin, M. Nohara, and H. Takagi, *Science* **294**, 2518 (2001).
- [51] Y. Noat, T. Cren, F. Debontridder, D. Roditchev, W. Sacks, P. Toulemonde, and A. San Miguel, *Phys. Rev. B* **82**, 014531 (2010).
- [52] I. Guillamón, H. Suderow, F. Guinea, and S. Vieira, *Phys. Rev. B* **77**, 134505 (2008).
- [53] E. Liebhaber, S. Acero González, R. Baba, G. Reecht, B. W. Heinrich, S. Rohlf, K. Rossnagel, F. von Oppen, and K. J. Franke, *Nano Lett.* **20**, 339 (2020).
- [54] G. C. Ménard, S. Guissart, C. Brun, S. Pons, V. S. Stolyarov, F. Debontridder, M. V. Leclerc, E. Janod, L. Cario, D. Roditchev, P. Simon, and T. Cren, *Nat. Phys.* **11**, 1013 (2015).
- [55] S. Kezilebieke, M. Dvorak, T. Ojanen, and P. Liljeroth, *Nano Lett.* **18**, 2311 (2018).
- [56] J. Senkpiel, C. Rubio-Verdú, M. Etkorn, R. Drost, L. M. Schoop, S. Dambach, C. Padurariu, B. Kubala, J. Ankerhold, C. R. Ast, and K. Kern, *Phys. Rev. B* **100**, 014502 (2019).
- [57] X. Yang, Y. Yuan, Y. Peng, E. Minamitani, L. Peng, J.-J. Xian, W.-H. Zhang, and Y.-S. Fu, *Nanoscale* **12**, 8174 (2020).
- [58] M. Ruby, Y. Peng, F. von Oppen, B. W. Heinrich, and K. J. Franke, *Phys. Rev. Lett.* **117**, 186801 (2016).
- [59] F. von Oppen and K. J. Franke, *Phys. Rev. B* **103**, 205424 (2021).
- [60] Supporting Information.
- [61] We do not preclude even longer-range interactions, but do not identify corresponding signatures within our resolution.
- [62] Next-nearest-neighbor coupling may also rationalize the unconventional energetic order of the number of nodal planes of the YSR wave functions in the trimer.
- [63] L. Schneider, P. Beck, J. Wiebe, and R. Wiesendanger, *Science Adv.* **7**, eabd7302 (2021).

SUPPLEMENTARY MATERIAL

THEORETICAL CONSIDERATIONS

The YSR states of the dimer are expected to exhibit both a shift and a splitting relative to the monomer. Our measurements show that the shift is comparable to (β) or even considerably larger (α) in magnitude than the splitting. Within a classical-spin model, the shift is of higher order in the coupling between the adatoms and hence generically smaller than the splitting. Specifically, in a tight-binding theory of the YSR dimer assuming classical spins, the shift is controlled by [1]

$$C = \int d\mathbf{r} K(\mathbf{r} + \mathbf{d}) \phi^\dagger(\mathbf{r}) \phi(\mathbf{r}), \quad (\text{S1})$$

while the splitting involves

$$D = \int d\mathbf{r} K(\mathbf{r}) \phi^\dagger(\mathbf{r}) \phi(\mathbf{r} + \mathbf{d}). \quad (\text{S2})$$

Here, $\phi(\mathbf{r})$ is the two-component spinor of the monomer YSR state (centered at $\mathbf{r} = \mathbf{0}$), \mathbf{d} denotes the distance vector between the adatoms constituting the dimer, and $K(\mathbf{r})$ is the exchange coupling between adatom and substrate electrons. When $|\mathbf{d}|$ is larger than the range of the exchange coupling $K(\mathbf{r})$, C and D are of different orders in the small overlap of the YSR wave functions of the dimer. While the shift $C \sim |\phi(\mathbf{d})|^2$ is quadratic in the overlap, the splitting $D \sim |\phi(\mathbf{d})|$ is linear.

In contrast, splitting and shifts are independent of one another within a quantum-spin model. While the splitting originates in the overlap of the YSR wave functions of the monomers, the shift involves the RKKY coupling between the adatom spins. For classical spins, the YSR excitation is merely associated with occupying a bound state with spin polarization antiparallel to the adatom spin. The impurity spin itself remains unchanged and hence there is no change in the RKKY energy due to the binding of the quasiparticle. For quantum spins, the YSR resonance comes with a change in the state of the impurity spin. For a spin- $\frac{1}{2}$ adatom, there is a finite energy gain from the RKKY coupling of two unscreened adatom spins, but no such energy gain when exciting the YSR excitation which screens one of the two spins. In the screened state, the adatom spin forms a singlet with the screening quasiparticle and can thus no longer align relative to another adatom spin. The YSR excitation energy of the dimer thus explicitly includes the RKKY coupling, resulting in a shift relative to the monomer. This mechanism underlying the shift is rooted in the different effective spins with and without screening quasiparticle and therefore clearly generalizes to higher spins.

The results for monomer, dimer, and trimer thus suggest that both the hybridization and the RKKY coupling of neighboring adatoms in our adatom chains are comparable to or smaller than the superconducting gap. To gain intuition for interpreting the observations of longer chains (but shorter than the scale on which the CDW becomes relevant), we consider a minimal model of $S = \frac{1}{2}$ adatoms coupled to single-site superconductors [2, 3],

$$H = \sum_j \left\{ \Delta \left[c_{j,\uparrow}^\dagger c_{j,\downarrow}^\dagger + \text{h.c.} \right] + \sum_{\sigma\sigma'} c_{j,\sigma}^\dagger [V\delta_{\sigma\sigma'} + K\mathbf{S}_j \cdot \mathbf{s}_{\sigma\sigma'}] c_{j,\sigma'} - t \sum_{\sigma} \left[c_{j,\sigma}^\dagger c_{j+1,\sigma} + \text{h.c.} \right] + J\mathbf{S}_j \cdot \mathbf{J} \cdot \mathbf{S}_{j+1} \right\}, \quad (\text{S3})$$

Here, \mathbf{S} denotes the $S = \frac{1}{2}$ adatom spins and \mathbf{J} the spin-spin coupling, including both the RKKY interaction (symmetric part of \mathbf{J}) and the Dzyaloshinsky-Moriya coupling (antisymmetric part). The exchange coupling between adatom spins and substrate electrons is taken to be isotropic and its strength is denoted by K . The substrate superconductor is reduced to a chain of single-site superconductors (annihilation operator $c_{j,\sigma}$ at site j of the chain) with pairing strength Δ . This description can be effectively thought of as projecting out the quasiparticle continuum and focusing on the subgap quasiparticles induced by the adatom spin. We also include a site energy V , which can be thought of as the strength of potential scattering of substrate electrons by the adatom. Finally, the hybridization of YSR states is captured by including a hopping term of strength t between neighboring single-site superconductors.

First consider the monomer [2]. Its eigenstates can be classified according to the fermion parity of the single-site superconductor. In the even-parity subspace (spanned by the empty and the doubly-occupied superconducting site), the monomer gains pairing energy Δ , but no exchange coupling K . (Both electronic states spanning the even-fermion-parity subspace are spin singlets.) In the odd-parity subspace (spanned by the two singly-occupied states of the superconducting site), the monomer does not gain pairing energy, but benefits from the exchange coupling due to singlet formation between the impurity spin and the substrate electron. Thus, the even-fermion-parity ground state

has energy $V - \sqrt{V^2 + \Delta^2}$, while the odd-fermion-parity state has energy $V - \frac{3K}{4}$. The energy of the YSR excitation is then given by

$$E_{\text{YSR}} = \sqrt{V^2 + \Delta^2} - \frac{3K}{4}. \quad (\text{S4})$$

For positive E_{YSR} , the monomer is in the doublet of free-spin ground states

$$|\pm\rangle = |S_z = \pm 1/2\rangle \otimes (u + vc_{\downarrow}^{\dagger}c_{\uparrow}^{\dagger})|\text{vac}\rangle, \quad (\text{S5})$$

as the adatom spin remains uncoupled to the substrate electrons. The YSR excitation excites the monomer into the screened-spin state

$$|0\rangle = (|\uparrow\downarrow\rangle - |\downarrow\uparrow\rangle)/\sqrt{2}, \quad (\text{S6})$$

in which the impurity spin forms a singlet with the substrate-electron spin. For negative E_{YSR} , the monomer is in the screened-spin ground state and the YSR excitation excites the free-spin doublet. In both cases, the energy of the YSR excitation is equal to $|E_{\text{YSR}}|$. Here, double arrows denote the impurity-spin state, whereas single arrows denote the spin state of the substrate electron,

$$|\sigma\rangle = c_{\sigma}^{\dagger}|\text{vac}\rangle = \gamma_{\sigma}^{\dagger}(u + vc_{\downarrow}^{\dagger}c_{\uparrow}^{\dagger})|\text{vac}\rangle. \quad (\text{S7})$$

The amplitudes

$$u = \sqrt{\frac{1}{2}\left(1 + \frac{V}{\sqrt{\Delta^2 + V^2}}\right)}, \quad v = \sqrt{\frac{1}{2}\left(1 - \frac{V}{\sqrt{\Delta^2 + V^2}}\right)} \quad (\text{S8})$$

denote the conventional electron and hole amplitudes u, v of BCS theory. They also enter the Bogoliubov operators

$$\gamma_{\sigma} = uc_{\sigma} + \sigma vc_{\sigma}^{\dagger} \quad (\text{S9})$$

of the subgap excitations.

Now consider coupled adatoms [3]. The experimental results suggest that both the RKKY coupling and the YSR hybridization are smaller than the superconducting gap. Here, we thus consider the limit $\Delta, K, V \gg t, J, E_{\text{YSR}}$. We can then restrict the Hilbert space by retaining only the singlets $|0_j\rangle$ (i.e., the screened-spin states) and the doublets $|\pm_j\rangle$ (i.e., the free-spin states) at all sites j of the chain. Within this restricted subspace, the spin-spin interaction J acts only between adjacent sites, which are both in the free-spin state. Moreover, the hybridization t changes the fermion parity of the two participating sites, thereby enabling two processes. Neighboring free-spin and screened-spin sites can exchange positions with effective amplitude $\tilde{t} = t(u^2 - v^2)/2 = tV/2\sqrt{\Delta^2 + V^2}$. Similarly, two adjacent free-spin sites with opposite spin can be converted into two screened sites (or vice versa) with amplitude $\tilde{\Delta} = tuv = t\Delta/2\sqrt{\Delta^2 + V^2}$.

We use exact diagonalization via the Lanczos scheme (with up to 300 states in the excited state sectors) to study the local single-particle spectral function

$$A_j(E) = \frac{\kappa}{\pi} \sum_{\sigma, \lambda} \left[\frac{|\langle \lambda | c_{j, \sigma}^{\dagger} | \text{g.s.} \rangle|^2}{\kappa^2 + (E - E_{\lambda} + E_{\text{g.s.}})^2} + \frac{|\langle \lambda | c_{j, \sigma} | \text{g.s.} \rangle|^2}{\kappa^2 + (E + E_{\lambda} - E_{\text{g.s.}})^2} \right]. \quad (\text{S10})$$

The local single-particle spectral function is expected to describe tunneling experiments using superconducting tips in the limit of weak tip-substrate tunneling. We note that our numerical results are restricted in a variety of ways relative to the experimental system. They are limited to spin- $\frac{1}{2}$ impurities, do not resolve the local YSR wave functions or accommodate specifics of the substrate due to the single-site approximation for the superconductor, are restricted to zero temperature, and involve a phenomenological broadening κ . The assumption of zero temperature is restrictive since we deduce a spin-spin interaction J which is comparable to temperature. Consequently, one expects that excited states of the spin chain, involving for instance domain walls within a ferromagnetically ordered chain can play a significant role in the experimental chains.

Within the quantum-spin model, energy bands and van Hove singularities tend to form in particular for ferromagnetic spin ordering. In this case, the tunneling electron changes the local spin state (by screening or unscreening the

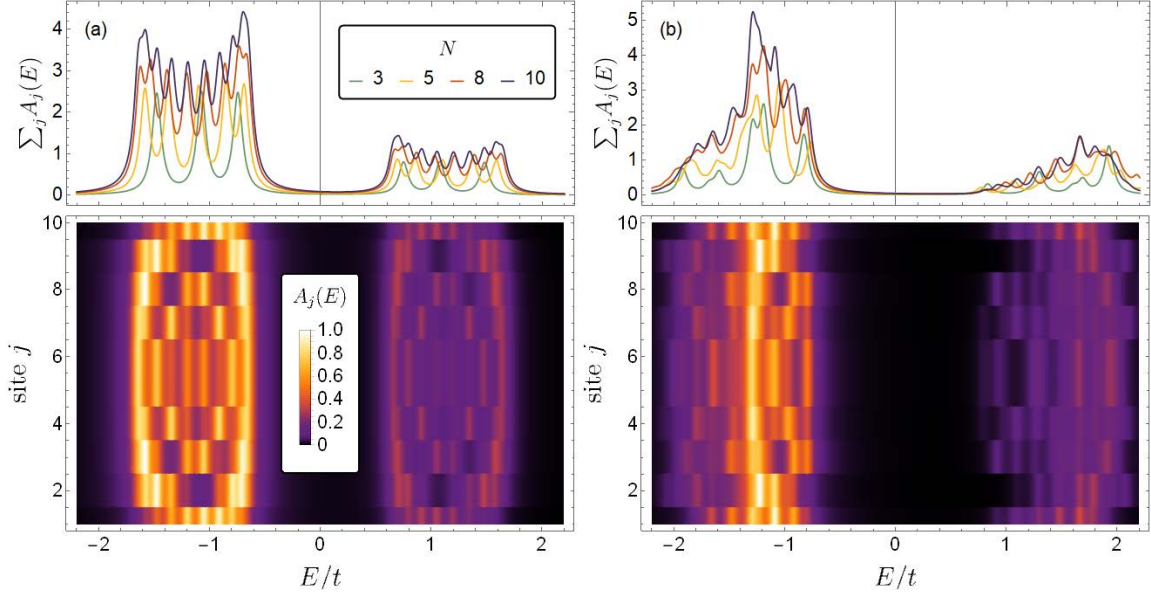


Figure S1. Local single-particle spectral density for a chain of spin- $\frac{1}{2}$ adatoms as modeled by the Hamiltonian in Eq. (S3). Top panels show single-particle spectral function integrated over the entire chain for different chain lengths N . Bottom panels exhibit spatially resolved spectral function for $N = 10$. (a) Ferromagnetic phase (fully unscreened phase) with $E_{\text{YSR}} = t$, $J = -0.3t$ and a miniscule magnetic field $B_z = 0.001t$. (b) Antiferromagnetic phase (fully unscreened phase) with $E_{\text{YSR}} = t$, $J = 0.3t$. Other parameters applicable to all panels: $V = -0.6\Delta$ (chosen such that $|v|^2 \simeq 3|u|^2$, similar to the experimental peak heights in Fig. 2, main text) and $\kappa = 0.05t$.

local spin), creating a mobile impurity in the spin chain. In the ferromagnetic phase, this impurity can hop to neighboring sites and effectively forms a single-particle band with van Hove singularities. Figure S1a shows the formation of the band as the number of adatoms N is increased, as seen in the local spectral function. The lower panel exhibits the local spectral function resolved all along a $N = 10$ chain. Qualitatively consistent with the experimental observation, one observes that there are incipient van Hove peaks at the two band edges. Presumably, these simulations assume better energy resolution than available in experiment, which overemphasizes the bending of the van Hove singularity along the chain due to the detailed node structure of the individual wave functions. This structure may be further reduced when including thermally excited spin states. The upper panel shows how the van Hove singularity emerges with increasing N , again qualitatively consistent with our experimental observations.

For contrast, Fig. S1b shows corresponding results for antiferromagnetic RKKY coupling. Unlike for ferromagnetic spin ordering, the excitation spectrum is not single-particle-like and does not exhibit pairs of van Hove singularities for any chain length. Single-particle bands and the emergence of van Hove singularities with increasing N are also observed when all spins are screened, see Fig. S2a. However, the experimental results indicate that the current system does not realize this limit (unscreened δ resonance as well as partially screened α band). Panels b and c of Fig. S2 show corresponding results for monomer YSR energies such that there is only partial screening. In this case, the single-particle spectral function exhibits a pair of peaks which are located at symmetric energies relative to the Fermi energy. These peaks are BCS coherence peaks induced by the singlet superconducting correlations $\tilde{\Delta}$. For unscreened δ resonance, this phase should not be realized in the experimental system, since ferromagnetic order suppresses the underlying singlet correlations. We also do not observe the well-developed gap around the Fermi energy which exists in this phase.

As discussed in the main text, we assume that the δ resonance is likely unscreened. However, this assignment (based on analyzing shifts of the YSR energy with adsorption position relative to the CDW) is less definitive than the ones for α - γ . We briefly comment on this issue in light of the observed band formation. When all YSR states are in the screened state in the monomer, the adatom spin is effectively fully screened in the monomer. Due to the quantum phase transition for the α resonance, we would then conclude that the adatom chains can effectively be viewed as partially filled spin- $\frac{1}{2}$ chain. In this case, there is a substantial region in the phase diagram in which the system is in a spin-singlet superconducting phase (in addition to the ferromagnetic phase discussed above) [3]. As seen in panels b and c of Fig. S2, the coherence peaks of this singlet superconductor naturally provide a single dominant peak which might be consistent with our observations of the α band. Indeed, as discussed in the main text, it is possible (though

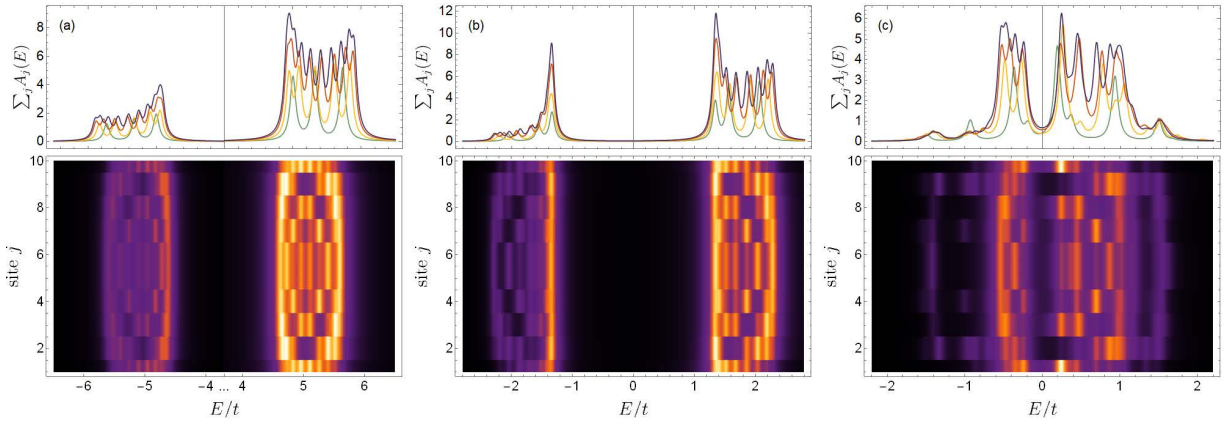


Figure S2. Local single-particle spectral density for a chain of spin- $\frac{1}{2}$ adatoms as modeled by the Hamiltonian in Eq. (S3). Top panels show single-particle spectral function integrated over the entire chain for different chain lengths N . Bottom panels exhibit spatially resolved spectral function for $N = 10$. (a) Fully screened phase with $E_{\text{YSR}} = -5t$. (b) Partially screened chain with incipient singlet superconducting correlations with $E_{\text{YSR}} = -1.5t$. (c) Singlet superconducting phase with $E_{\text{YSR}} = 0$. Other parameters applicable to all panels: $V = -0.6\Delta$ (chosen such that $|v|^2 \simeq 3|u|^2$, similar to the experimental peak heights in Fig. 2, main text), $J = 0$, and $\kappa = 0.05t$. Color code in top panels as in Fig. S1.

less likely) that this resonance leads to symmetric peaks about the Fermi energy. However, an interpretation of this observation in terms of coherence peaks of a spin-singlet superconductor seems unlikely since we do not observe the associated gap around the Fermi energy. Note in particular that according to the top panels, the zero-temperature spectral function does not exhibit any structure within this gap for any chain length N . Moreover, the observation of two peaks for the β band is much less natural in such a spin-singlet superconductor, as its excitation spectrum does not exhibit single-particle character. Based on these considerations, we conclude that the observations on adatom chains support our identification of the δ resonance as unscreened.

ADDITIONAL EXPERIMENTAL DATA

Adsorption sites and incommensurate CDW

Fe atoms deposited at low temperature on the clean NbSe₂ surface adsorb in two distinct sites. They can be distinguished by their different apparent height (Fig. S3a) and identified as sitting in the two different hollow sites of the terminating Se layer, which differ by the presence (metal-centered, MC) or absence (hollow-centered, HC) of a Nb atom underneath. The YSR states from the Fe atoms in the different adsorption sites differ substantially [4]. Here, we investigate and build up chains from Fe atoms on the HC sites only.

The incommensurate nature of the CDW with a periodicity of $\gtrsim 3a \times 3a$ [5] (see white arrow in Fig. S3a) is reflected in an additional modulation to the atomic corrugation in the STM images. When the maximum of the CDW is located on a hollow site of the Se layer (hollow-centered, HC), the topographic pattern appears with a three-petaled shape (yellow area in Fig. S3a and Fig. S3b). In contrast, when the CDW maximum lies on top of a Se atom (chalcogen-centered, CC), the STM image is petalless (red area in Fig. S3a and Fig. S3c). Due to the incommensurability of the CDW, the patterns smoothly transform into one another.

Atom manipulation using a superconducting Nb tip

All measurements were performed with a superconducting Nb tip fabricated by indenting a NbTi-tip into a superconducting Nb sample until a sharp stable tip apex exhibiting the full Nb gap of $\Delta \approx 1.55$ meV is achieved. To construct the adatom chains, controlled manipulation of the Fe atoms is required. The atoms could be positioned in a very precise manner after placing the STM tip in their close vicinity and dragging them across the surface, while applying small bias voltages (\sim mV) and currents in the nA-regime (exact values depend on the tip apex).

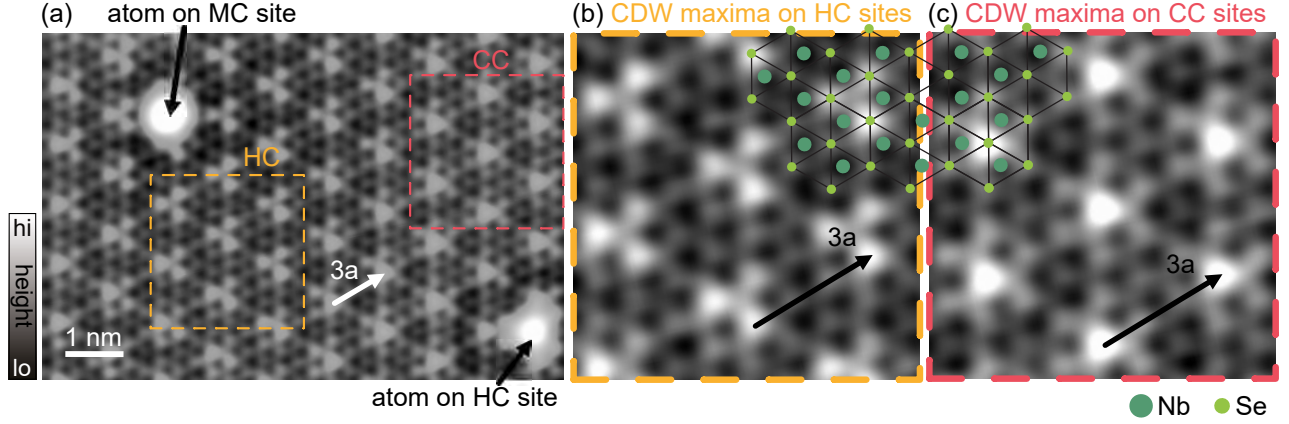


Figure S3. (a) Atomic resolution topography (constant-current mode, set point: 500 mV, 80 pA). (b) and (c) are zooms into the areas marked in (a). Arrows indicate one CDW period ($\approx 3a$). The overlaid grid shows the terminating Se-layer (bright green) and the Nb layer beneath (dark green).

Deconvolution and fitting procedure

Due to the superconducting properties of the STM tip, the dI/dV spectra are a convolution of the density of states of tip and substrate. To extract the density of states of the substrate, we numerically deconvolve the spectra as described in the supplementary information to Ref. [4]. Deconvolved spectra of the monomer, dimer and trimer (original spectra in Fig. 2a,c,e of the main manuscript) are shown in Fig. S4a. To determine the shift and split of the α - and β -derived YSR states in the dimer and trimer structure, we symmetrized the deconvolved spectra with respect to zero energy and then fitted them with the appropriate number of Gaussian peaks using the following equation:

$$\text{DOS}(E) = D_0 + \sum_{i=1}^N \left(A_i e^{-(E \pm E_{\alpha_i})^2 / (2\sigma^2)} + B_i e^{-(E \pm E_{\beta_i})^2 / (2\sigma^2)} \right). \quad (\text{S11})$$

Here, D_0 is an intensity offset, A_i (B_i) are the (symmetric) amplitudes of the α - (β -)derived resonances and σ is the width of the Gaussian peaks. The number of split YSR states depends on the number of atoms N in the hybridized structure, being two states in the dimer ($\alpha^{\text{d0,d1}}$ and $\beta^{\text{d0,d1}}$) and three YSR states in the trimer ($\alpha^{\text{t0,t1,t2}}$ and $\beta^{\text{t0,t1,t2}}$). As shown in the main manuscript, the YSR states exhibit strong spatial intensity variations, with some peaks being hardly visible in some spectra. The most reliable determination of all peak positions thus follows from a detailed analysis of a set of spectra from the line profiles in Fig. 2b,d,f of the main text. Several spectra were fitted and the fit results of the YSR energies were averaged. The error bars of the YSR energies were determined from the standard deviation of the fit, the error margin of the energy gap of the tip, the modulation voltage of the lock-in, and the sampling interval of the data used for the deconvolution.

Figure 3e (main part) compiles the resulting peak positions in the monomer, dimer and trimer. Table S1 summarizes the energy splittings $D_{\alpha,\beta}$ and shifts $C_{\alpha,\beta}$ in the hybridized structures relative to the monomer.

An example of a fitted trace of a trimer is shown in Fig. S4c (position of the original spectrum marked by the arrow and dashed line in Fig. S4b). The gray trace is the symmetrized density of states. The fit according to Eq. S11 is shown in yellow and the individual Gaussian peaks are shown (for positive energies only) in color. The fit yields reliable values for α^{t0} , α^{t1} and β^{t2} , as they are well separated peaks. In contrast, as discussed in the main text, α^{t2} and β^{t1} strongly overlap leading to one broad resonance (full width half maximum of $\approx 100 \mu\text{eV}$). The peak corresponding to β^{t0} is very close to the quasiparticle coherence peaks. For these reasons, we added additional error margins of $\pm 50 \mu\text{eV}$ to the latter three resonances.

Influence of the Fe atoms to the CDW

As described in the main manuscript, an 11-atom chain can be built in such a way that all Fe atoms sit on maxima of the CDW. This contrasts the smooth variation of the CDW and indicates that the Fe atoms may help to lock the phase of the CDW. Upon further extension of the chain, the locking is not operable anymore and the atoms cannot

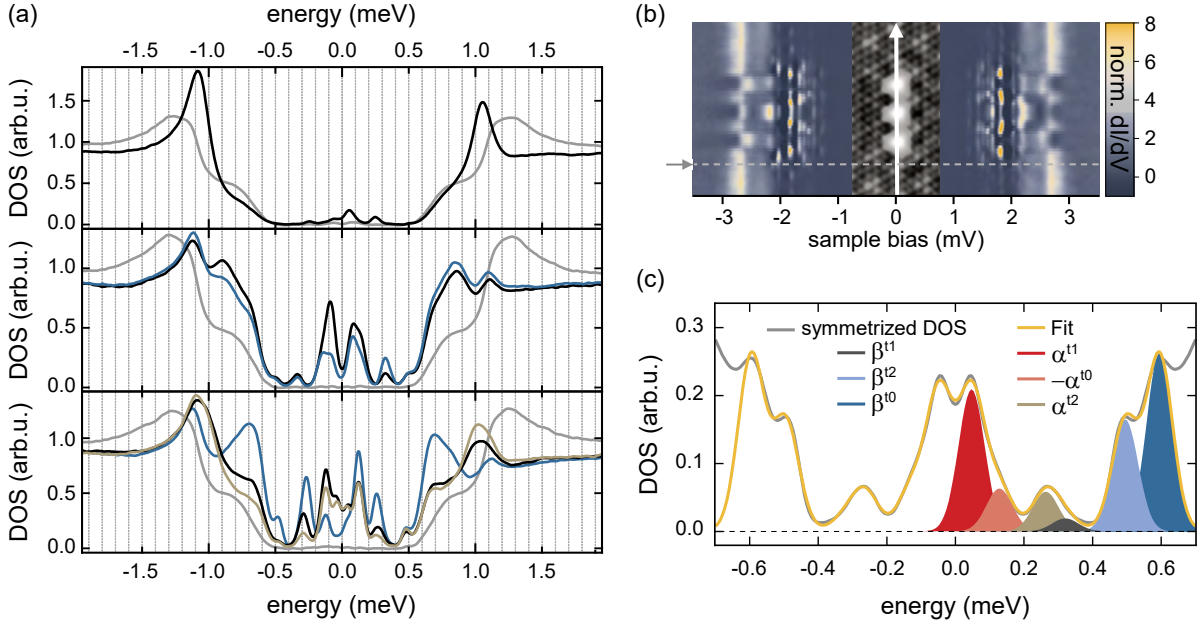


Figure S4. (a) Deconvolved data of Fig. 2a,c,e. For the deconvolution $\Delta_{\text{tip}} = 1.55$ meV and a depairing factor of $\Gamma = 5$ μeV were used. (b) Data reproduced from Fig. 2f. The gray dashed line marks the position of the spectrum that is symmetrized in (c) (gray line). The fit (yellow) and the individual Gaussian peaks (only at positive energy) are shown in red and blue colors for the α - and β -derived states, respectively.

	$ D_{\alpha}(\mu\text{eV}) $	$ D_{\beta}(\mu\text{eV}) $	$C_{\alpha}(\mu\text{eV})$	$C_{\beta}(\mu\text{eV})$
dimer	69 ± 33	173 ± 33	$+184 \pm 29$	-160 ± 29
trimer	388 ± 62	286 ± 79	$+14 \pm 33$	-201 ± 36

Table S1. Results for the splits $D_{\alpha,\beta}$ and shifts $C_{\alpha,\beta}$ (relative to the monomer) of the hybrid α - and β -states of the dimer and trimer obtained from Fig. 3e main part.

sit on the CDW maxima. From this length on, the smoothly varying phase along the atomic lattice leads to shifts of the YSR band structure. Importantly, during the manipulation and extension of the chain up to a chain length of $N = 30$ atoms, the CDW did not change abruptly. In contrast, upon attachment of the 31st atom, an abrupt change occurred in the CDW (compare Fig. S5a and b). This change is most clearly expressed in a change of the dI/dV spectra. While the 30-atom chain exhibits the smooth variations of van Hove singularities toward the chain's terminations, the 31-atom chain shows two distinct areas of YSR bands. Close inspection of the CDW phase reveals that the atoms in the area marked by a white arrow are now located on minima of the CDW (Fig. S5a,d). These observations suggest that the Fe atoms favor adsorption sites on the maxima or minima of the CDW and thus push the CDW into the respective phase. However, when too much energy is stored in the locked CDW, stress is released by an abrupt switching of the CDW.

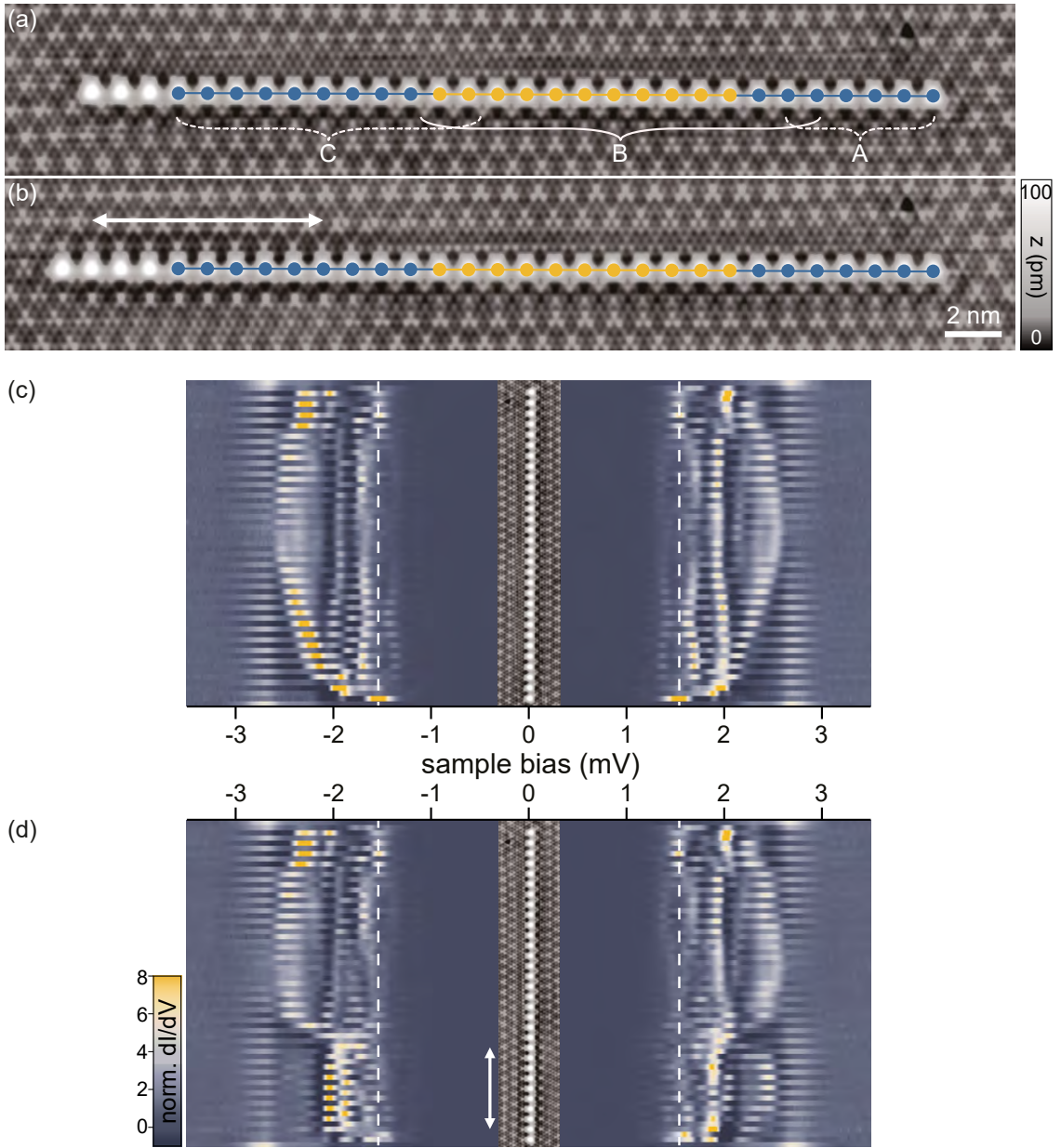


Figure S5. (a,b) Constant-current topography of the 30-atom chain (a) and 31-atom chain (b) recorded at a set point of 500 mV, 80 pA. The former 11-atom (27-atom) chains are indicated in yellow (blue). The white arrow marks the section of the 31-atom chain where atoms are located on a CDW minimum. (c,d) Line profiles of normalized dI/dV spectra recorded along the 30-atom chain (c) and 31-atom chain (d) (constant-height mode, feedback opened at 700 pA, 5 mV with a modulation of 15 μV). The arrow marks the same section as in (b). Dashed lines indicate the tip gap.

Additional dI/dV maps

In the main manuscript, we have presented selected dI/dV maps of monomers, dimer, trimers and an extended 27-atom chain, which helped identifying the nature of the YSR states. This section provides additional data, which corroborate the assignments in the main text.

Figure S6a-c complements the dI/dV maps presented in Fig.3 of the main manuscript with the opposite bias polarity. Additionally, Fig. S6d,e show dI/dV maps of the thermally activated α -derived resonances at $eV_{\text{YSR}} = \mp|\Delta_{\text{tip}} - E_{\text{YSR}}|$. These data support the identification of the α - and β -derived states by their distinct symmetries

and presence/absence of nodal planes. Especially the assignment of both α states of the dimer to be at the other bias polarity becomes clear when inspecting the thermal maps. Further, the two nodal planes of α^{t2} are more pronounced at negative bias. Some similar features among the β states are highlighted in white (arrows, dashed lines).

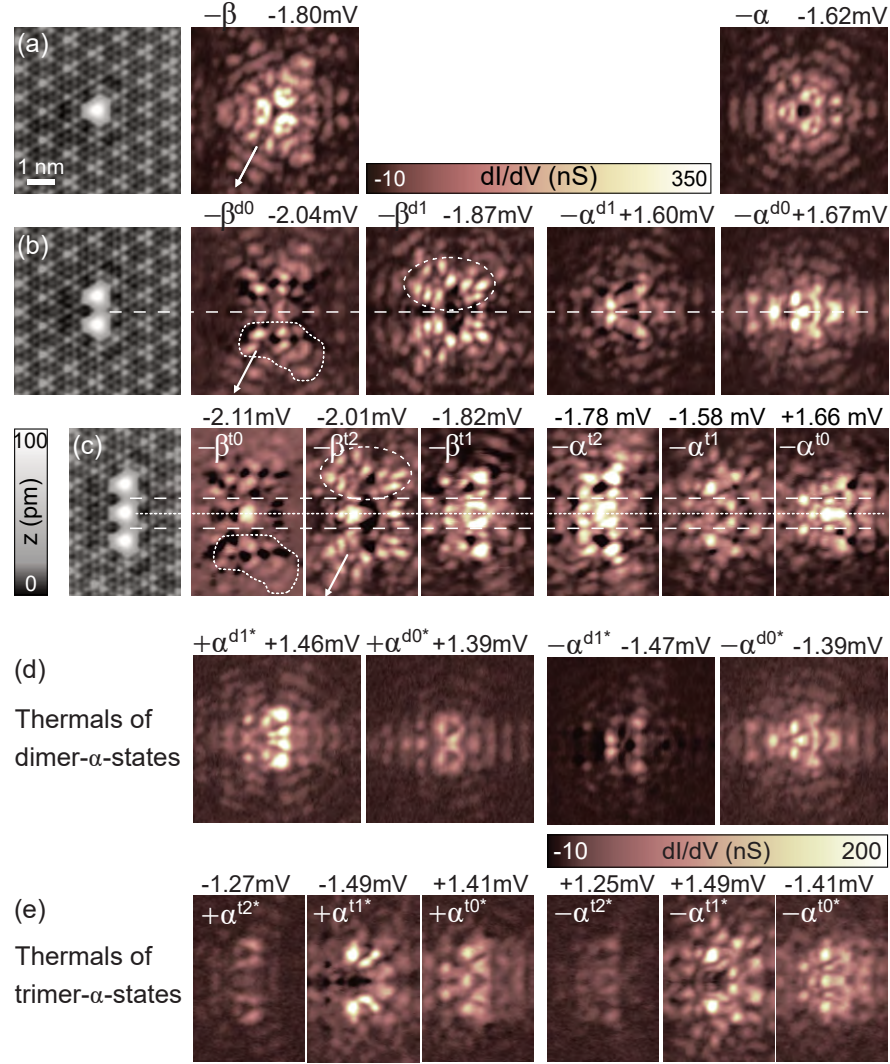


Figure S6. Complementary data of Fig. 3 in the main part. (a-c) STM topographies (constant-current mode with set point 500mV , 80pA) of one to three Fe atoms with spacing of $3a$ in the left. Corresponding constant-contour dI/dV maps of the (hybridized) YSR states in the monomer (top row), dimer (middle row) and trimer (bottom row). Bias voltages are given above each panel ($V_{\text{YSR}} = \pm|\Delta_{\text{tip}} + E_{\text{YSR}}|/e$ with $\Delta_{\text{tip}} \approx 1.55\text{meV}$). Constant-contour feedback set point is 250pA , 5mV and the modulation is $15\mu\text{V}$. (d,e) Constant-contour maps (same parameters as in a-c) of the thermally activated α -states of the dimer (d) and the trimer (e).

Figures S7 and S8 show additional dI/dV maps at various energies for chain lengths between 4 and 11 atoms. The maps reflect the character of the hybrid wave functions and their intensity distributions along shorter chains and further highlight the extended nature of the YSR bands for increasing chain length ($N > 5$). We can identify the origin of the bands at larger chain length by structural elements common to the single atom, short and long chains. For example, we find signatures of the β -derived state within the coherence peaks always around ≈ 2.15 mV and around 1.95 mV as indicated by the blue arrows. States deep within the gap arise from α -states as suggested by comparing the shapes to the α -trimer states (Figs. 3c main part and S6).

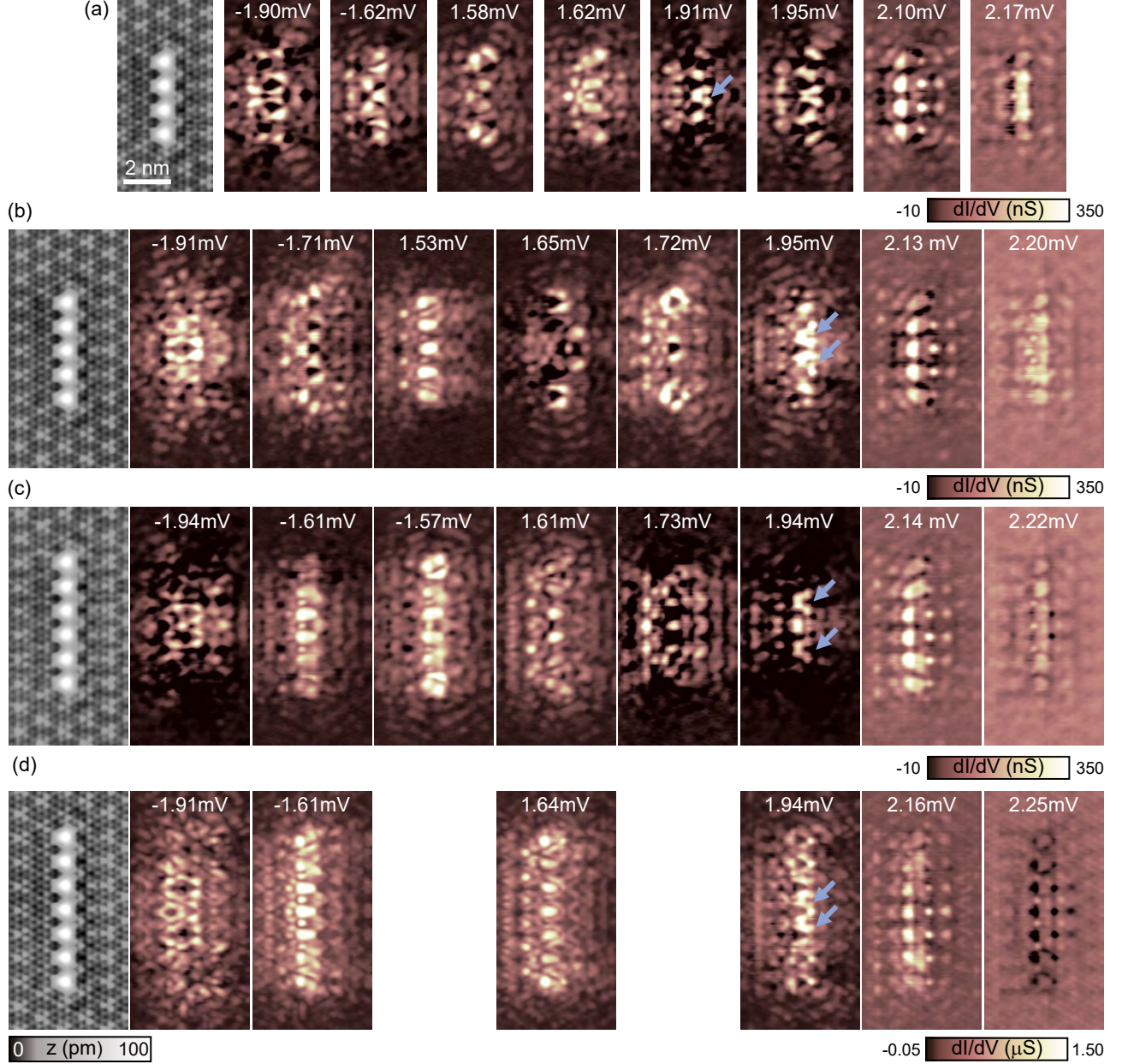


Figure S7. Complementary data to Fig. 4a-d of the main manuscript. (a-d) STM topographies (constant-current mode with set point 100 pA, 10 mV) of the 4-, 5-, 6- and 7-atom chains with spacing of $3a$ on the left. Corresponding constant-contour dI/dV maps at selected bias voltages (values indicated in the panels) on the right. Constant-contour feedback was opened at 250 pA, 5 mV (a-c) or 700 pA, 5 mV (d) and a modulation of 15 μ V was used ($\Delta_{\text{tip}} \approx 1.55$ mV).

As mentioned in the main text there is a zero-energy end state ($\Delta_{\text{tip}} \approx 1.55 \text{ mV}$) in the 10-atom chain. However, as can be inferred from the line spectra in Fig. 4g,h in the main paper, this state is shifted to slightly higher energies at the 11-atom chain (1.58 meV). dI/dV maps shown in Fig. S8 sustain this interpretation.

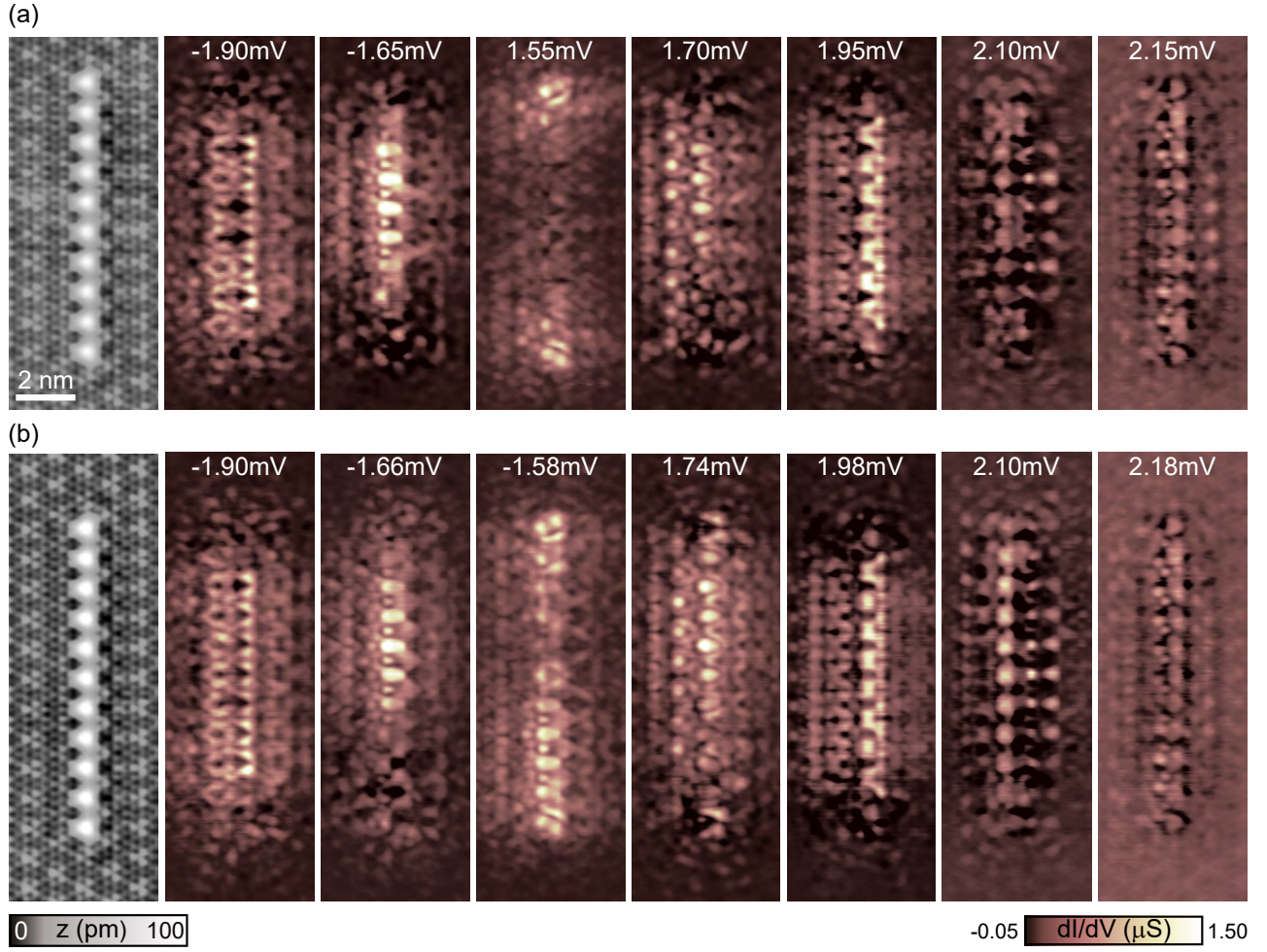


Figure S8. Complementary data to Fig. 4g,h of the main manuscript. (a,b) STM topographies (constant-current mode with set point 100 pA, 10 mV) of the 10- and 11-atom chains with spacing of $3a$ in the left. Corresponding constant-contour dI/dV maps at selected bias voltages (values indicated in the panels) on the right. Constant-contour feedback was opened at 700 pA, 5 mV and a modulation of 15 μV was used ($\Delta_{\text{tip}} \approx 1.55 \text{ meV}$).

Figures S9 and S10 complement the data of the dI/dV maps of the 27-atom chain (Fig. 5 of the main text) showing the energetic and spatial evolution of the YSR bands as discussed in the main text.

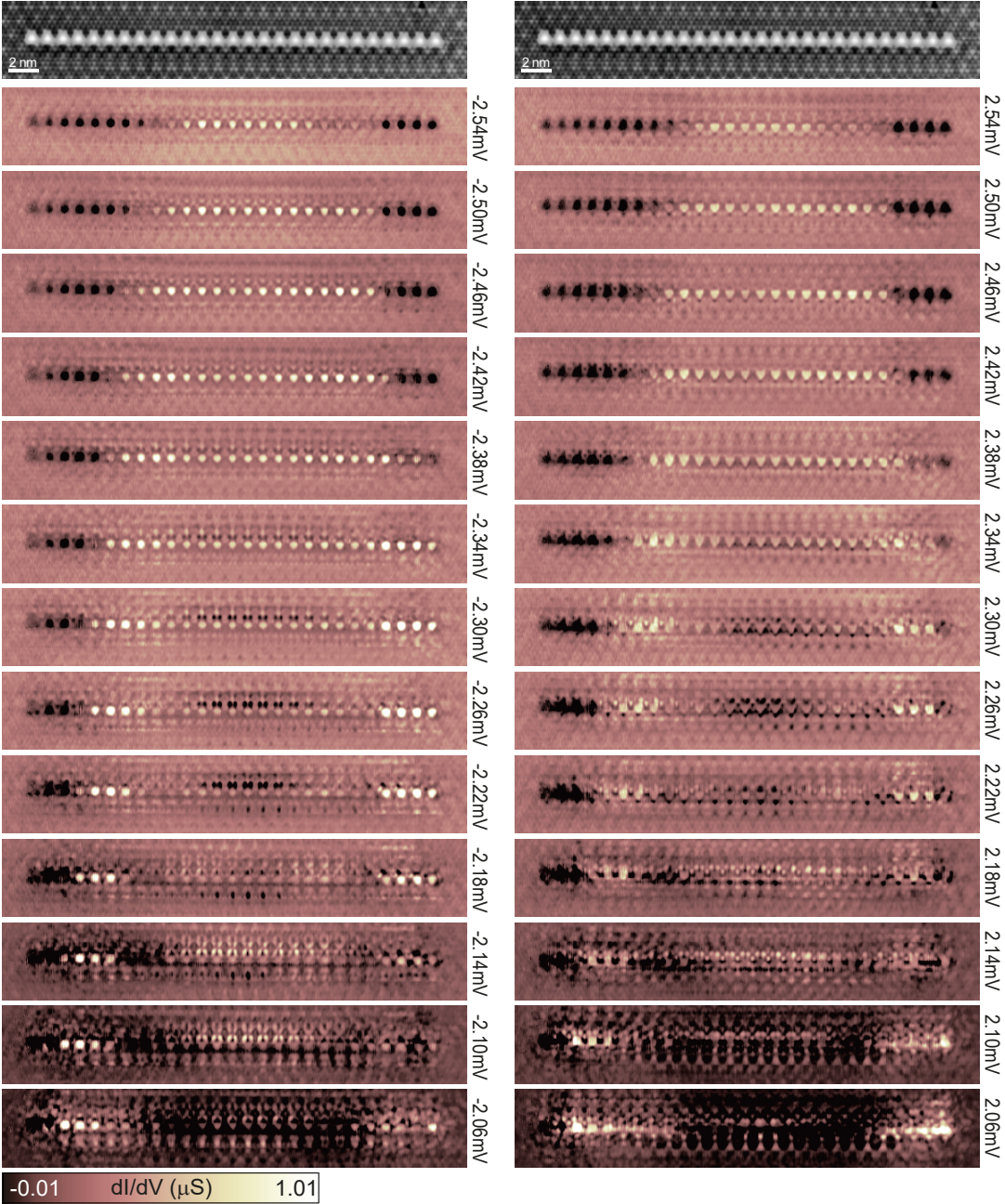


Figure S9. Complementary data to Fig. 5 in the main part. Constant-contour dI/dV maps recorded at the voltages given next to each panel ($\Delta_{\text{tip}} \approx 1.55$ meV). Feedback was opened at 700 pA, 5 mV and a modulation of 15 μ V was used. Topography can be found in the top (set point: 100 pA, 10 mV).

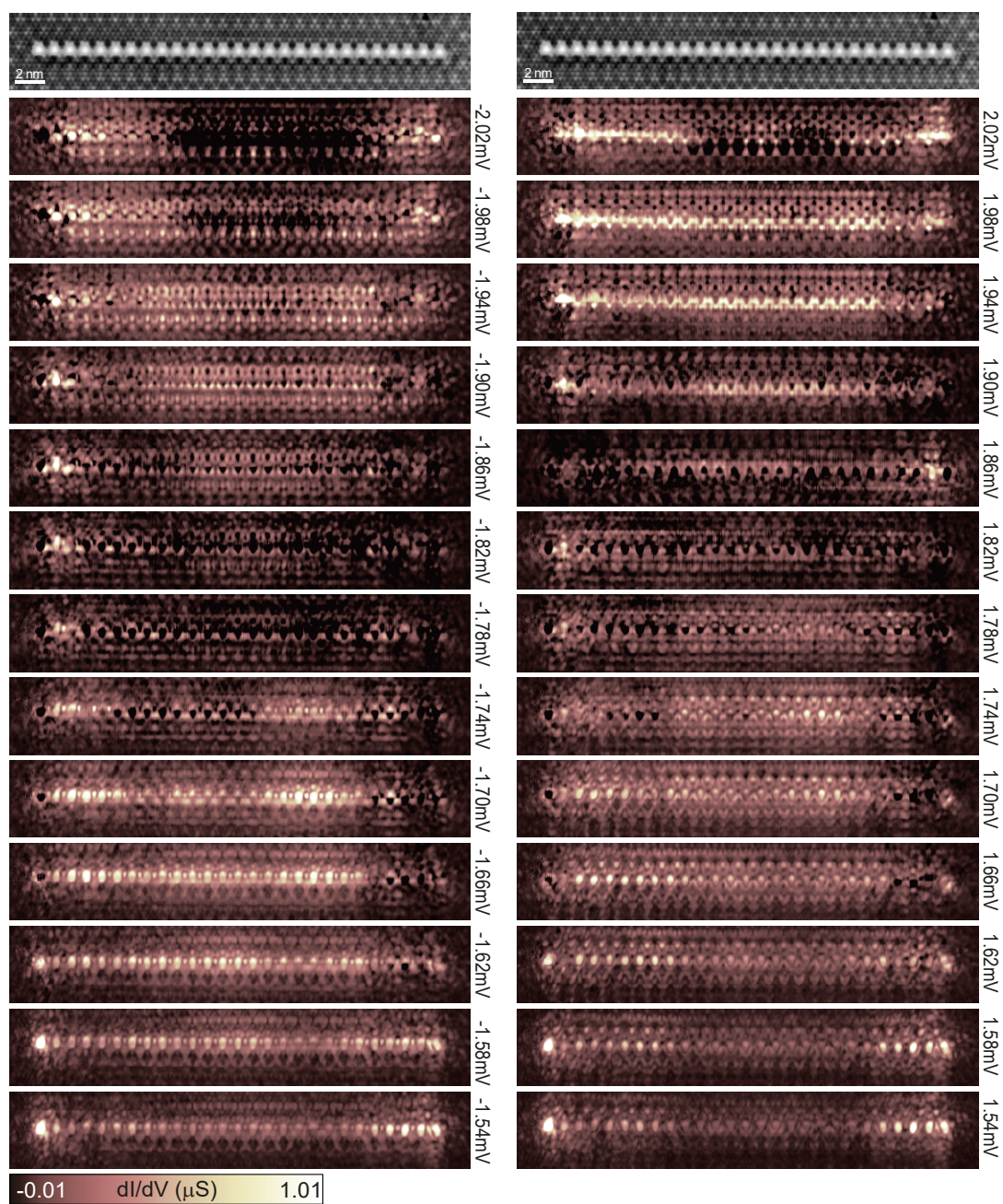


Figure S10. Complementary data to Fig. 5 in the main part. Constant-contour dI/dV maps recorded at the voltages given next to each panel ($\Delta_{\text{tip}} \approx 1.55$ meV). Feedback was opened at 700 pA, 5 mV and a modulation of 15 μV was used. Topography can be found in the top (set point: 100 pA, 10 mV).

Figure S11 shows dI/dV maps of the 51-atom chain at selected energies, which highlight the localization of the YSR bands in the different regions. In particular, region A shows the down-shifted bands at the chain's termination, region B shows the bands of a chain with Fe atoms sitting on CDW maxima, region C represents the abrupt transition between the Fe atoms located on maxima (region B) and minima (region D) of the CDW, region E shows again band shifts at the chain termination.

Removal of three Fe atoms in region C leads to two separate chains (as the CDW starts to distort also on the left end, we also removed one atom there). dI/dV maps taken at the same energies as for the uninterrupted chain show very similar intensity distributions (compare Fig. S11 and Fig. S12). Regions A, B and D, E of the complete 51-atom chain can thus be interpreted as two non-interacting sub-chains.

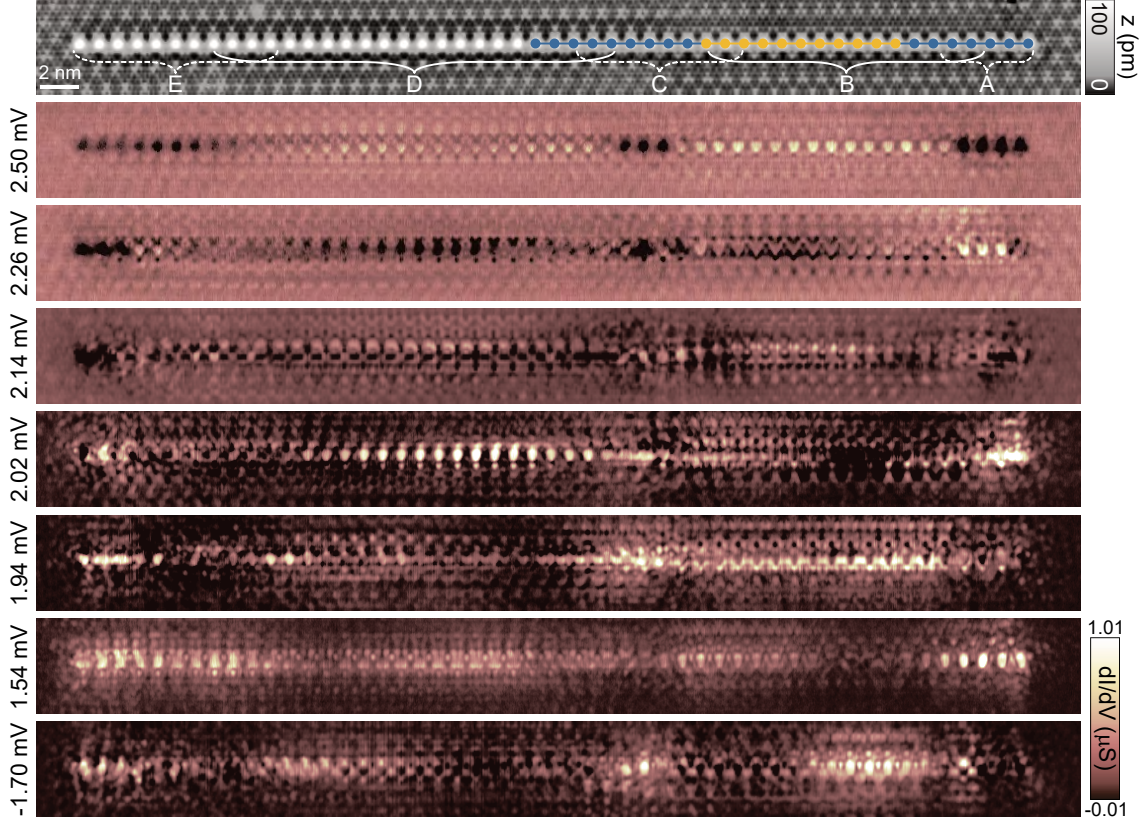


Figure S11. Selected constant-contour dI/dV maps recorded on the 51-atom chain (Fig. 6 in the main part) at the voltages given at the left to each panel ($\Delta_{\text{tip}} \approx 1.55$ meV). Feedback was opened at 700 pA, 5 mV and a modulation of 15 μ V was used. Topography can be found in the top (set point: 500 mV, 80 pA). The former 11- (27-) atom chain is indicated in yellow (blue).

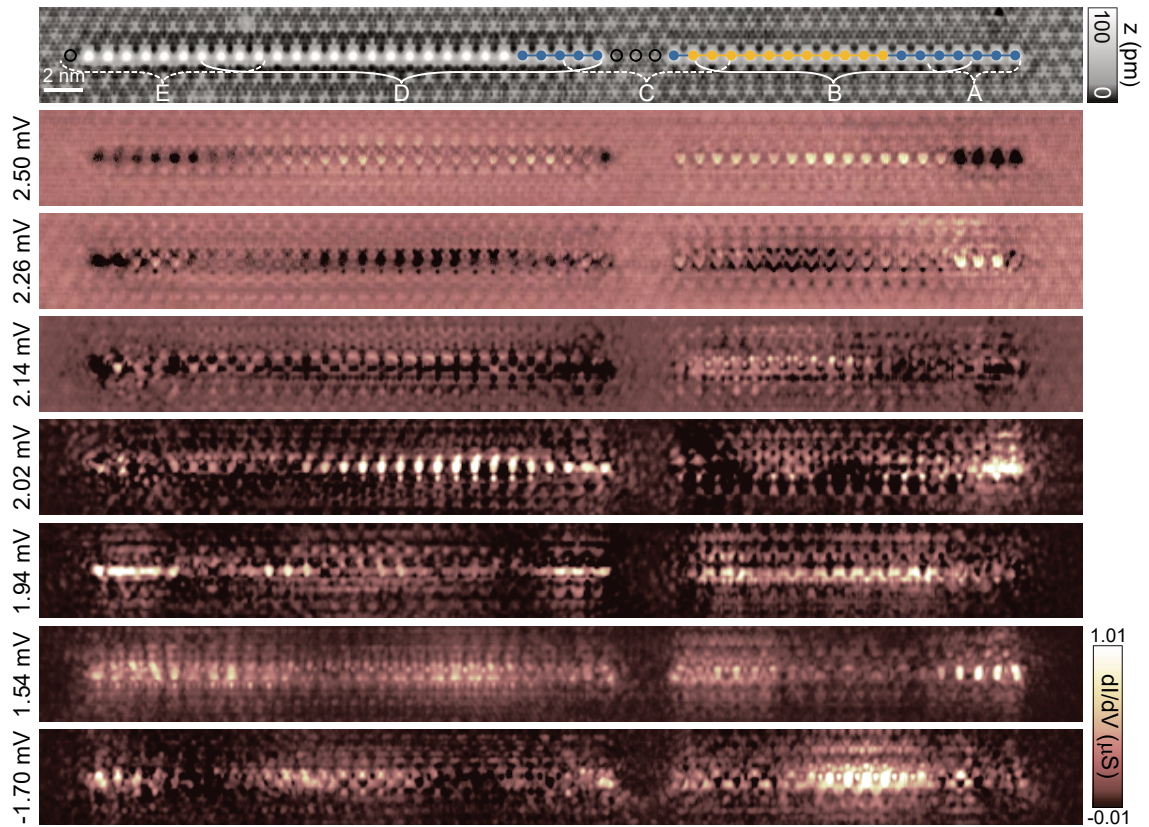


Figure S12. Selected constant-contour dI/dV maps recorded on the former 51-atom chain (Fig. 5 in the main part) after removal of a few atoms (black circles). Voltages given on the left to each panel ($\Delta_{\text{tip}} \approx 1.55$ meV). Data in the different sections are very similar to the 51-atom chain. Feedback was opened at 700 pA, 5 mV and a modulation of 15 μ V was used. Topography can be found in the top (set point: 500 mV, 80 pA).

-
- [1] M. Ruby, B. W. Heinrich, Y. Peng, F. von Oppen, and K. J. Franke, *Phys. Rev. Lett.* **120**, 156803 (2018).
 - [2] F. von Oppen and K. J. Franke, *Phys. Rev. B* **103**, 205424 (2021).
 - [3] J. F. Steiner, C. Mora, K. J. Franke, and F. von Oppen, (2021), [arXiv:2107.00031 \[cond-mat.supr-con\]](https://arxiv.org/abs/2107.00031).
 - [4] E. Liebhaber, S. Acero González, R. Baba, G. Reecht, B. W. Heinrich, S. Rohlf, K. Rossnagel, F. von Oppen, and K. J. Franke, *Nano Lett.* **20**, 339 (2020).
 - [5] A. Soumyanarayanan, M. M. Yee, Y. He, J. van Wezel, D. J. Rahn, K. Rossnagel, E. W. Hudson, M. R. Norman, and J. E. Hoffman, *Proc. Natl. Acad. Sci.* **110**, 1623 (2013).